

The corona and upper transition region of ϵ Eridani

J.-U. Ness^{1,2*} and C. Jordan¹

¹*Department of Physics, Rudolf Peierls Centre for Theoretical Physics, University of Oxford, 1 Keble Road, Oxford OX1 3NP, UK*

²*School of Earth and Space Exploration, Arizona State University, Tempe, AZ 85287-1404, USA*

Accepted ; Received 24 October 2018

ABSTRACT

We present analyses of observations of ϵ Eridani (K2 V) made with the Low Energy Transmission Grating Spectrometer on *Chandra* and the *Extreme Ultraviolet Explorer*, supplemented by observations made with the Space Telescope Imaging Spectrograph, the *Far Ultraviolet Spectroscopic Explorer* and the Reflection Grating Spectrometer on *XMM-Newton*. The observed emission lines are used to find relative element abundances, to place limits on the electron densities and pressures and to determine the mean apparent emission measure distribution. As in the previous paper by Sim & Jordan (2003a), the mean emitting area as a function of the electron temperature is derived by comparisons with a theoretical emission measure distribution found from energy balance arguments. The final model has a coronal temperature of 3.4×10^6 K, an electron pressure of 1.3×10^{16} cm⁻³K at $T_e = 2 \times 10^5$ K and an area filling factor of 0.14 at 3.2×10^5 K. We discuss a number of issues concerning the atomic data currently available. Our analyses are based mainly on the latest version of CHIANTI (v5.2). We conclude that the Ne/O relative abundance is 0.30, larger than that recommended from solar studies, and that there is no convincing evidence for enhanced coronal abundances of elements with low first ionization potentials.

Key words: stars: coronae - stars: individual (ϵ Eridani) - stars: late-type - stars: abundances.

1 INTRODUCTION

ϵ Eri (K2 V) is a nearby dwarf star that has been observed over a wide spectral range, from the infrared to X-ray wavelengths. Its fundamental parameters have been discussed by Drake & Smith (1993), where references to earlier work can be found, and more recently by Di Folco et al. (2004) and Allende Prieto et al. (2004). Di Folco et al. (2004) have derived the diameter of ϵ Eri from interferometric measurements and have also made models to check the self-consistency of their adopted parameters. A more recent measurement by Di Folco et al. (2007) gives a radius that is smaller by only 0.008 R_\odot . The values of the parameters adopted here are given in Table 1 and are from Di Folco et al. (2004), although these are also consistent with those found by Drake & Smith (1993), to within the combined uncertainties. Compared with the Sun, ϵ Eri has a shorter rotational period (11.68 d) (Donahue et al. 1996), a larger spatially averaged magnetic field (165 G) (Rüedi et al. 1997) and larger stellar surface emission line fluxes. It is, therefore, ideal for studies of a stellar outer atmosphere under conditions of higher mean magnetic activity than the Sun.

Observations with *IRAS* showed that ϵ Eri has an infrared excess, indicating the presence of dust; more recently a planet and a debris disk have been detected (Hatzes et al. 2000; Greaves et al. 2005). Further studies of the dust have been made by Di Folco et al. (2007). Combining the above rotational period with $v \sin i = 1.7$ km s⁻¹ and $R_* = 0.743 R_\odot$ (Di Folco et al. 2004), leads to $i = 32^\circ$, similar to the value of 25° suggested by Greaves et al. (2005) for the inclination of the debris disc to the plane of the sky.

Here we make use of observations at ultraviolet to X-ray wavelengths, as summarized in Table 2. In previous work we used observations with the Space Telescope Imaging Spectrograph (STIS) on the *Hubble Space Telescope* to identify forbidden lines of Fe XII (Jordan et al. 2001a) and to determine the electron pressure (P_e) in the transition region (Jordan et al. 2001b). Including observations with the *Far Ultraviolet Spectroscopic Explorer* (*FUSE*), we have modelled the chromosphere and transition region, up to an electron temperature (T_e) of $\simeq 3 \times 10^5$ K (Sim & Jordan 2005).

Observations with the *Extreme Ultraviolet Explorer* (*EUVE*) have been analysed by a number of authors. Schmitt et al. (1996) used lines of iron to derive the emission measure distribution (EMD) at above $T_e \simeq 6 \times 10^5$ K and also placed limits on the electron density (n_e) in the upper transition region from lines of Fe XIII and Fe XIV.

* E-mail: Jan-Uwe.Ness@asu.edu

Laming et al. (1996) used the same spectra to derive emission measures from lines of a range of elements and concluded that if any trends in abundances with the first ionization potential (FIP) were present, they were not significantly larger than in the solar corona. Sanz-Forcada et al. (2003) included further *EUV*E spectra and also derived the EMD. They found much larger values of n_e from lines of Fe XIX and Fe XXI that are now superseded. Sim & Jordan (2003a) used the line fluxes measured by Schmitt et al. (1996) to derive the EMD from the iron lines alone, adopting a more recent (smaller) value of the interstellar absorption by Dring et al. (1997) and using CHIANTI (v4) (Dere et al. 1997; Young et al. 2003) for line excitation atomic data. They compared the apparent EMD with that calculated from an energy balance in which the net thermal conductive flux was set equal to the local radiative energy loss and hence derived the fractional emitting area as a function of T_e ($\simeq 0.2$ at 2×10^5 K).

High-resolution X-ray observations of ϵ Eri have been made with both the Low Energy Transmission Grating Spectrograph (LETGS) on *Chandra* and the Reflection Grating Spectrometer (RGS) on *XMM-Newton*. The former observations have been reduced and analysed by Sanz-Forcada et al. (2004) and Wood & Linsky (2006), who derived the EMD and relative element abundances, making use of the Astrophysical Plasma Emission Database (APED v1.3) (Smith et al. 2001) and CHIANTI (v4.2), respectively. Because there have been changes in the atomic data available, we have made our own analysis of the above spectra and the *EUV*E spectra, using CHIANTI (v5.2) (Landi et al. 2006). We have also made our own measurements of the X-ray line fluxes. ϵ Eri was included in a survey of stellar coronal densities by Ness et al. (2002), using LETGS spectra, and in a study of coronal opacities by Ness et al. (2003a), using LETGS and RGS spectra. Comparisons with these earlier results are made in later sections.

The first aim of the present work is to use all the available observations and up-to-date atomic data to derive the mean EMD, the relative element abundances and the electron densities and pressures. The mean EMD is then used in conjunction with new theoretical EMDs to refine the earlier values of the mean emitting areas.

Section 2 describes the X-ray observations used and the data reduction. Limits on n_e and P_e are discussed in Section 3, since these are required in deciding on the identification of some lines and in the analysis of some line fluxes. The identifications of particular lines are discussed in Section 4, in conjunction with the emission measures derived and some issues related to the atomic data. Section 5 describes how the mean EMD and the relative element abundances were derived. In Section 6, the theoretical EMD and the fractional areas occupied by the emitting regions are derived, using the method set out in Sim & Jordan (2003a). Our main conclusions are summarized in Section 7.

2 OBSERVATIONS AND DATA REDUCTION

2.1 X-ray observations

We use the *Chandra* LETGS spectra (ObsID 1869) that had an exposure time of 105.3 ks. We have also examined the

Table 1. Stellar parameters adopted.

| Distance ^a (pc) | Mass ^b (M_\odot) | Radius ^b (R_\odot) | $\log g_*$ ^b | $\log N_{\text{H}}^c$ |
|-------------------------------|------------------------------------|--------------------------------------|-------------------------|-----------------------|
| 3.218 | 0.9 ± 0.1 | 0.743 ± 0.01 | 4.65 ± 0.1 | 17.88 ± 0.07 |

^a The *Hipparcos* catalogue ESA (1997).

^b Di Folco et al. (2004); g_* in cm s^{-2} . Allende Prieto et al. (2004) give a value of $\log g_* = 4.621$.

^c Dring et al. (1997); N_{H} in cm^{-2} .

spectra obtained with the *XMM-Newton* RGS instrument (ObsID 0112880501) that have an exposure time of 13 ks. These spectra are available from the *Chandra* and *XMM-Newton* archives.

The LETGS projects the dispersed spectrum onto a microchannel plate detector. The detector is placed behind the grating in a manner such that the non-dispersed photons (zeroth order) are recorded in the middle of the detector, with the two dispersion directions appearing as spectra in the plus and minus directions. There is overlap between the first-order spectra and the various higher-order spectra of shorter wavelengths and care must be taken to exclude higher order lines or to account for line blending when this occurs in important first-order lines. In the lists of lines given in Tables 3 and 4, purely higher-order lines are excluded and blends with first-order lines are noted.

2.2 Data reduction

We extracted the LETGS spectra on the plus and minus sides separately and calculated the effective areas using the standard CIAO tools (v3.2). The measurement of line fluxes was carried out with the CORA program developed by Ness & Wichmann (2002). This accounts for the particular problems of low-count photon statistics (see, e.g., Ness et al. 2001). After trying several approaches we used a fixed line width (FWHM- Full width at half maximum) of 0.060 Å, since intrinsic stellar line widths are not resolvable.

As noted by others (see the extensive discussion in Chung et al. 2004), the apparent wavelengths of lines can differ between the plus and minus sides, leading to larger linewidths when the spectra in the plus and minus side spectra are summed. The line fluxes given in Tables 3 and about half of those in 4 are derived from the summed spectra, using variable line widths of between 0.053 and 0.080 Å, although the larger widths usually occur only at wavelengths above 90 Å. We have checked that these fluxes do not differ significantly from the averages of the fluxes in the individual plus and minus side spectra. Some lines are not observed, or are poorly observed, in one of the two spectra. In this case only one spectrum is used; the wavelengths of such lines are given in italic script in Table 4. We also give the effective areas adopted so that the original count rates can be recovered.

All the line fluxes have then been corrected for absorption in the interstellar medium (ISM) using a hydrogen column density of $\log N_{\text{H}}(\text{cm}^{-2}) = 17.88$ from Dring et al. (1997), lower than that used by Sanz-Forcada et al. (2003) who adopted a value of 18.1. The absorption model also includes He I, He II and other abundant elements. Uncertainties in the line fluxes arise not only from the statistical measurement errors calculated by the CORA program, but also

Table 2. Dates of observations used.

| Instrument | Date |
|-------------|--------------------|
| LETGS | 2001 March 21 |
| RGS | 2003 January 19 |
| <i>EUVE</i> | 1993 October 22/23 |
| STIS | 2000 March 9 |
| <i>FUSE</i> | 2000 December 8 |

from the line widths adopted and the source continuum. The line widths in the LETGS spectra can be approximated by Moffat profiles (Lorentzians with an exponent $\beta = 2.4$; Drake 2004). The source continuum can be accounted for in CORA by adding a background (in counts $\text{s}^{-1} \text{\AA}^{-1}$) to the line templates. By varying the source background we found that in many cases, the dominant source of the uncertainty in line fluxes arises from the choice of the source background. The specific case of the lines of O VII is discussed in Section 3.

The APED (Smith et al. 2001) and CHIANTI (v5.2) (Landi et al. 2006) data bases were consulted in making the line identifications (see also Section 4). Lines marked with *b* are possibly blended but the identification of the main additional contributor is not certain and these lines are not used in the analyses of line fluxes. Blending between first-order lines occurs in several important cases. The methods used to find the relative contributions are discussed in Section 4. Fluxes were measured for all lines, but since our aim is to establish a reliable EMD a number of weak lines are not included in Tables 3 and 4, unless they have particular significance for our studies. A fuller list of lines present has been published by Sanz-Forcada et al. (2004).

There are systematic differences between laboratory and observed wavelengths above about 80 \AA (where the observed wavelengths are too large), owing to the treatment of detector plate gaps (see Chung et al. 2004). Since we are not analyzing line shifts and are using only well identified lines in this region, we have not attempted to correct these wavelengths.

In reducing the RGS1 and RGS2 spectra we used Lorentzian line profiles to approximate the instrumental line profiles and used a fixed FWHM of 0.06 \AA . The only use we have made of these spectra is in comparisons between LETGS and RGS fluxes where line blending is not significant, because the instrumental wings to the lines prevents accurate deblending.

2.3 Other observations; potential variability of ϵ Eri

In later sections we will be using spectra obtained with the *EUVE*, STIS and *FUSE*. Table 2 gives the dates on which these observations were made.

Baliunas et al. (1983, 1995) have studied the Ca II emission lines over various time scales and find no clear single activity cycle. The monthly variations in the S-index cover a total amplitude of $\simeq 24$ per cent, so that the chromospheric emission does not show substantial variations. Sim & Jordan (2005) found no significant differences between the fluxes in transition region lines observed with the *International Ultraviolet Explorer (IUE)* in 1981 and with the STIS in 2000.

Table 3. Line fluxes measured from the LETG spectrum of ϵ Eri. See Section 2 for details.

| λ (\AA) | Flux ^a | Λ_{eff} (cm^2) | λ^e (\AA) | Ion | Transition |
|-------------------------------|-------------------|---|---------------------------------|----------|---|
| 6.65 | 8.39 ± 2.77 | 44.1 | 6.65 | Si XIII | $1s^2 1S_0-1s2p^1 P_1$ |
| -6.74 | | | 6.69 | Si XIII | $1s^2 1S_0-1s2p^3 P_{1,2}$ |
| | | | 6.74 | Si XIII | $1s^2 1S_0-1s2s^3 S_1$ |
| 8.42 | 3.68 ± 0.66 | 38.2 | 8.42 | Mg XII | $1s^2 2S_{1/2}-2p^2 P_{1/2,3/2}$ |
| 9.17 | 12.6 ± 2.5 | 32.5 | 9.17 | Mg XI | $1s^2 1S_0-1s2p^1 P_1$ |
| -9.31 | | | 9.23 | Mg XI | $1s^2 1S_0-1s2p^3 P_{1,2}$ |
| | | | 9.31 | Mg XI | $1s^2 1S_0-1s2s^3 S_1$ |
| 10.23 | 4.20 ± 0.75 | 28.7 | 10.24 | Ne X | $1s^2 2S_{1/2}-3p^2 P_{1/2,3/2}$ |
| 11.27 | 4.69 ± 0.74 | 28.5 | 11.25 | Fe XVII | $2p^6 1S_0-2p^5 (2P)5d^3 D_1^b$ |
| 11.55 | 5.58 ± 0.75 | 29.1 | 11.55 | Ne IX | $2s^2 1S_0-1s3p^1 P_1^b$ |
| 12.14 | 29.5 ± 1.4 | 28.7 | 12.14 | Ne X | $1s^2 2S_{1/2}-2p^2 P_{1/2,3/2}$ |
| | $\sim 27\%^c$ | | 12.12 | Fe XVII | $2p^6 1S_0-2p^5 4d^1 P_1$ |
| 12.29 | 7.18 ± 0.80 | 28.5 | 12.26 | Fe XVII | $2p^6 1S_0-2p^5 (2P)4d^3 D_1$ |
| 13.45 | 22.9 ± 1.05^d | 29.4 | 13.45 | Ne IX | $1s^2 1S_0-1s2p^1 P_1$ |
| 13.55 | 7.57 ± 0.60^d | 29.4 | 13.55 | Ne IX | $1s^2 1S_0-1s2p^3 P_{1,2}$ |
| 13.70 | 16.1 ± 0.9^d | 29.4 | 13.70 | Ne IX | $1s^2 1S_0-1s2s^3 S_1$ |
| 13.83 | 3.67 ± 0.41 | 29.4 | 13.82 | Fe XVII | $2s^2 2p^6 1S_0-2s2p^6 3p^1 P_1^b$ |
| 14.21 | 10.9 ± 0.9 | 29.5 | 14.21 | Fe XVIII | $2p^5 2P_{3/2}-2p^4 (1D)3d^2 D_{5/2}$ |
| | -14.26 | | 14.26 | Fe XVIII | $2p^5 2P_{3/2}-2p^4 3d^2 S_{1/2}^b$ |
| 14.38 | 4.19 ± 0.69 | 29.6 | 14.37 | Fe XVIII | $2p^5 2P_{3/2}-2p^4 (3P)3d^2 D_{5/2}^b$ |
| 15.02 | 52.1 ± 1.6 | 30.3 | 15.02 | Fe XVII | $2p^6 1S_0-2p^5 (2P)3d^1 P_1$ |
| 15.19 | 7.98 ± 0.84 | 30.4 | 15.18 | O VIII | $1s^2 2S_{1/2}-4p^2 P_{1/2,3/2}^b$ |
| 15.27 | 21.8 ± 1.1 | 30.5 | 15.26 | O VIII | $2p^6 1S_0-2p^5 (2P)3d^3 D_1^b$ |
| 16.01 | 17.1 ± 1.0 | 29.9 | 16.01 | O VIII | $1s^2 2S_{1/2}-3p^2 P_{1/2,3/2}$ |
| | $\sim 19\%^c$ | | 16.01 | Fe XVIII | $2p^5 2P_{3/2}-2p^4 (3P)3s^2 P_{3/2}$ |
| 16.09 | 5.80 ± 0.67 | 30.2 | 16.08 | Fe XVIII | $2p^5 2P_{3/2}-2p^4 (3P)3s^4 P_{5/2}$ |
| 16.77 | 30.4 ± 1.2 | 30.6 | 16.78 | Fe XVII | $2p^6 1S_0-2p^5 (2P)3s^1 P_1$ |
| 17.05 | 77.0 ± 3.0 | 25.7 | 17.05 | Fe XVII | $2p^6 1S_0-2p^5 (2P)3s^3 P_1$ |
| | -17.10 | | 17.10 | Fe XVII | $2p^6 1S_0-2p^5 (2P)3s^3 P_2$ |
| 18.63 | 7.79 ± 1.26 | 26.3 | 18.63 | O VII | $1s^2 1S_0-1s3p^1 P_1^b$ |
| 18.97 | 88.2 ± 1.9 | 26.5 | 18.97 | O VIII | $1s^2 2S_{1/2}-2p^2 P_{1/2,3/2}$ |
| 21.61 | 41.5 ± 1.5 | 17.3 | 21.60 | O VII | $1s^2 1S_0-1s2p^1 P_1$ |
| 21.81 | 9.60 ± 0.83 | 17.0 | 21.81 | O VII | $1s^2 1S_0-1s2p^3 P_{1,2}$ |
| 22.11 | 27.3 ± 1.3 | 17.0 | 22.10 | O VII | $1s^2 1S_0-1s2s^3 S_1$ |
| 24.79 | 10.8 ± 0.9 | 16.8 | 24.78 | N VII | $1s^2 2S_{1/2}-2p^2 P_{1/2,3/2}$ |
| 28.47 | 3.53 ± 0.55 | 15.6 | 28.47 | C VI | $1s^2 2S_{1/2}-3p^2 P_{1/2,3/2}$ |
| 28.79 | 3.56 ± 0.55 | 15.3 | 28.79 | N VI | $1s^2 1S_0-1s2p^1 P_1$ |
| 29.09 | < 2.50 | 15.0 | 29.08 | N VI | $1s^2 1S_0-1s2p^3 P_{1,2}$ |
| 29.54 | < 2.80 | 14.1 | 29.53 | N VI | $1s^2 1S_0-1s2s^3 S_1$ |
| 30.45 | 4.37 ± 0.64 | 12.1 | 30.47 | S XIV | $2s^2 2S_{1/2}-3p^2 P_{1/2,3/2}$ |
| | | | 30.45 | Ca XI | $2p^6 1S_0-2p^5 3d^1 P_1$ |
| 32.24 | 2.47 ± 0.52 | 13.5 | 32.24 | S XIII | $2s^2 1S_0-2s3p^1 P_1^b$ |
| 32.56 | 3.70 ± 0.55 | 13.3 | 32.56 | S XIV | $2p^2 P_{3/2}-3d^2 D_{3/2,5/2}$ |
| 33.55 | 2.47 ± 0.49 | 12.8 | 33.55 | S XIV | $2p^2 P_{3/2}-3s^2 S_{1/2}$ |
| 33.74 | 17.1 ± 1.0 | 12.8 | 33.74 | C VI | $1s^2 2S_{1/2}-2p^2 P_{1/2,3/2}$ |
| 35.69 | 4.17 ± 0.55 | 12.3 | 35.67 | S XIII | $2s2p^1 P_1-2s3d^1 D_2^b$ |
| 37.61 | 2.14 ± 0.49 | 10.4 | 37.60 | S XIII | $2s2p^1 P_1-2s3s^1 S_0^b$ |
| 40.27 | 3.35 ± 0.78^d | 5.5 | 40.27 | C V | $1s^2 1S_0-1s2p^1 P_1$ |
| 43.76 | 2.89 ± 0.27 | 25.9 | 43.76 | Si XI | $2s^2 1S_0-2s3p^1 P_1^b$ |
| 44.02 | 3.75 ± 0.29 | 26.1 | 44.02 | Si XII | $2p^2 P_{1/2}-3d^2 D_{3/2}^b$ |
| 44.17 | 5.47 ± 0.34 | 26.1 | 44.18 | Si XII | $2p^2 P_{3/2}-3d^2 D_{3/2,5/2}$ |
| 45.51 | 1.30 ± 0.21 | 25.7 | 45.52 | Si XII | $2p^2 P_{1/2}-3s^2 S_{1/2}$ |
| 45.69 | 2.01 ± 0.24 | 25.6 | 45.69 | Si XII | $2p^2 P_{3/2}-3s^2 S_{1/2}$ |

^a Fluxes are in $10^{-14} \text{ erg cm}^{-2} \text{ s}^{-1}$.

^b Likely to be blended.

^c The percentage contribution to the total flux given.

^d Fluxes after deblending.

^e Wavelengths from CHIANTI (v5.2).

Regarding variations in emission from the upper transition region and corona, Sanz-Forcada et al. (2003), using the *EUVE* Deep Survey Imager, observed similar mean levels of counts in the 80 \AA to 180 \AA passband in 1993 and 1995, although some variations of the order of ± 30 per cent were observed over a time interval of hours. Similarly, Sanz-Forcada et al. (2004) show light curves obtained from

Table 4. Continuation from Table 3.

| λ (Å) | Flux ^a | A_{eff} (cm ²) | λ^c (Å) | Ion | Transition |
|--------------------------|-------------------|--|--------------------|-----------------|---|
| 49.21 | 3.79 ± 0.29 | 24.4 | 49.22 | Si XI | $2s2p\ ^1P_1 - 2s3d\ ^1D_2$ |
| <i>50.36^d</i> | 4.96 ± 0.49 | 10.9 | 50.36 | Fe XVI | $3s\ ^2S_{1/2} - 4p\ ^2P_{3/2}$ |
| | $\sim 29\%c$ | | 50.34 | 3^{rd} | order 16.78 Å |
| <i>50.55</i> | 3.75 ± 0.44 | 10.9 | 50.52 | Si X | $2p\ ^2P_{1/2} - 3d\ ^2D_{3/2}$ |
| | $\sim 51\%c$ | | 50.57 | Fe XVI | $3s\ ^2S_{1/2} - 4p\ ^2P_{1/2}$ |
| <i>50.69</i> | 2.83 ± 0.39 | 10.9 | 50.69 | Si X | $2p\ ^2P_{3/2} - 3d\ ^2D_{5/2,3/2}$ |
| <i>52.32</i> | 2.16 ± 0.36 | 10.4 | 52.30 | Si XI | $2s2p\ ^1P_1 - 2s3s\ ^1S_0$ |
| <i>52.90</i> | 2.24 ± 0.37 | 10.4 | 52.91 | Fe XV | $3s\ ^2S_0 - 3s4p\ ^1P_1$ |
| <i>54.14</i> | 2.84 ± 0.38 | 10.2 | 54.13 | Fe XVI | $3p\ ^2P_{1/2} - 4d\ ^2D_{3/2}$ |
| <i>54.72</i> | 4.78 ± 0.46 | 10.1 | 54.71 | Fe XVI | $3p\ ^2P_{3/2} - 4d\ ^2D_{5/2,3/2}$ |
| <i>57.90</i> | 2.11 ± 0.48 | 9.2 | 57.92 | Mg X | $2s\ ^2S_{1/2} - 3p\ ^2P_{1/2,3/2}$ |
| <i>59.40</i> | 2.97 ± 0.44 | 8.0 | 59.40 | Fe XV | $3s3p\ ^1P_1 - 3s4d\ ^1D_2$ |
| <i>62.88</i> | 2.73 ± 0.43 | 7.7 | 62.87 | Fe XVI | $3p\ ^2P_{1/2} - 4s\ ^2S_{1/2}$ |
| <i>63.15</i> | 1.07 ± 0.34 | 7.7 | 63.15 | Mg X | $2p\ ^2P_{1/2} - 3d\ ^2D_{3/2}$ |
| <i>63.31</i> | 2.80 ± 0.44 | 7.7 | 63.31 | Mg X | $2p\ ^2P_{3/2} - 3d\ ^2D_{5/2,3/2}$ |
| <i>63.73</i> | 6.20 ± 0.57 | 7.6 | 63.71 | Fe XVI | $3p\ ^2P_{3/2} - 4s\ ^2S_{1/2}$ |
| <i>65.86</i> | 1.06 ± 0.37 | 7.3 | 65.85 | Mg X | $2p\ ^2P_{3/2} - 3s\ ^2S_{1/2}$ |
| <i>66.25</i> | 3.78 ± 0.51 | 7.2 | 66.25 | Fe XVI | $3d\ ^2D_{3/2} - 4f\ ^2F_{5/2}$ |
| | | | 66.30 | 3^{rd} | order 22.10 Å |
| <i>66.35</i> | 5.91 ± 0.60 | 7.1 | 66.36 | Fe XVI | $3d\ ^2D_{5/2} - 4f\ ^2F_{7/2,5/2}$ |
| 69.60 | 1.07 ± 0.25 | 14.3 | | b | |
| 69.68 | 5.47 ± 0.41 | 14.3 | 69.68 | Fe XV | $3s3p\ ^1P_1 - 3s4s\ ^1S_0$ |
| 72.32 | < 1.14 | 13.5 | 72.31 | Mg IX | $2s2p\ ^1P_1 - 2s3d\ ^1D_2$ |
| 73.48 | 2.70 ± 0.53 | 13.0 | 73.47 | Fe XV | $3s3d\ ^1D_2 - 3s4f\ ^1F_3$ |
| | | | 73.48 | Ne VIII | $2p\ ^2P_{1/2} - 4d\ ^2D_{3/2}$ |
| 76.04 | 1.32 ± 0.27 | 12.2 | 76.02 | Fe XIV | $3d\ ^2D_{3/2} - 4f\ ^2F_{5/2,3/2}$ |
| 76.13 | 1.21 ± 0.27 | 12.2 | 76.15 | Fe XIV | $3d\ ^2D_{5/2} - 4f\ ^2F_{7/2}$ |
| 76.53 | 1.61 ± 0.28 | 12.0 | | ? | |
| | | | 76.50 | Fe XVI | $3d\ ^2D_{5/2} - 4p\ ^2P_{3/2}$ ^b |
| 77.74 | < 0.63 | 11.7 | 77.74 | Mg IX | $2s2p\ ^1P_1 - 2s3s\ ^1S_0$ |
| 88.11 | 5.07 ± 0.89 | 9.5 | 88.08 | Ne VIII | $2s\ ^2S_{1/2} - 3p\ ^2P_{3/2}$ |
| <i>-88.15</i> | | | 88.12 | Ne VIII | $2s\ ^2S_{1/2} - 3p\ ^2P_{1/2}$ |
| 93.97 | 7.08 ± 0.51 | 8.8 | 93.92 | Fe XVIII | $2s\ ^2P_5^5 - 2p\ ^5P_{3/2} - 2s2p\ ^6S_{1/2}$ |
| 98.15 | 1.68 ± 0.34 | 7.6 | 98.12 | Ne VIII | $2p\ ^2P_{1/2} - 3d\ ^2D_{3/2}$ |
| 98.28 | 3.90 ± 0.45 | 7.6 | 98.26 | Ne VIII | $2p\ ^2P_{3/2} - 3d\ ^2D_{5/2}$ |
| | | | 98.27 | Ne VIII | $2p\ ^2P_{3/2} - 3d\ ^2D_{3/2}$ |
| 101.62 | 1.43 ± 0.36 | 7.1 | 101.55 | Fe XIX | $2s\ ^2P_4^3 - 2p\ ^5P_3$ |
| 104.00 | 2.57 ± 0.41 | 6.9 | 103.94 | Fe XVIII | $2s\ ^2P_5^5 - 2p\ ^5P_{1/2} - 2s2p\ ^6S_{1/2}$ |
| 108.42 | 2.54 ± 0.41 | 6.8 | 108.36 | Fe XIX | $2s\ ^2P_4^3 - 2p\ ^5P_2$ |
| 132.93 | < 4 | 3.9 | 132.84 | Fe XX | $2s\ ^2P_3^4 - 3p\ ^4S_{3/2} - 2s2p\ ^4P_{5/2}$ |
| 141.09 | 2.57 ± 0.57 | 4.0 | 141.04 | Ca XII | $2s\ ^2P_5^5 - 2p\ ^5P_{3/2} - 2s2p\ ^6S_{1/2}$ |
| 150.16 | < 2.17 | 3.6 | 150.12 | O VI | $2s\ ^2S_{1/2} - 3p\ ^2P_{3/2,1/2}$ |
| 152.25 | 2.82 ± 0.57 | 3.6 | 152.15 | Ni XII | $3p\ ^5P_{3/2} - 3p\ ^4(3P)3d\ ^2D_{5/2}$ |
| | | | | Ni XII | $3p\ ^5P_{3/2} - 3p\ ^4(3P)3d\ ^2P_{1/2}$ |
| 154.25 | 1.57 ± 0.50 | 3.6 | 154.16 | Ni XII | $3p\ ^5P_{3/2} - 3p\ ^4(3P)3d\ ^2D_{3/2}$ |
| <i>171.17</i> | 13.0 ± 1.7 | 1.2 | 171.07 | Fe IX | $3p\ ^6S_0 - 3p\ ^5d\ ^1P_1$ |

^a Fluxes are in 10^{-14} erg cm⁻² s⁻¹.^b Likely to be blended.^c The percentage contribution to the total flux given.^d Wavelengths in italics indicate flux measurements on one side only.^e Wavelengths from CHIANTI (v5.2).

the LETGS observations that exhibit variations amounting to about ± 21 per cent over 28 hours. The only systematic difference between the LETGS and *EUVE* observations is that the fluxes of lines of iron in stages of ionization greater than Fe XVIII are lower in the LETGS spectra, suggesting that the star had less hot active region material at that time. For the lines observed in both the RGS1 and RGS2 spectra, the mean RGS fluxes are on average a factor of only 1.06 larger than those derived from the LETGS spectra. We conclude that significant uncertainties should not be introduced by combining observations made on different dates.

3 THE ELECTRON PRESSURE

Jordan et al. (2001b) measured a number of density-sensitive line flux ratios in their STIS spectrum of ϵ Eri and used these to investigate P_e and to assess the available atomic data (in CHIANTI v3.01 and relevant papers). Throughout the present work we define $P_e = N_e T_e$ cm⁻³ K. Values of $\log P_e = 15.69 \pm 0.1$ at $\log T_e \simeq 4.5$ and $\simeq 15.67$ at $\log T_e \simeq 5.15$ were obtained from the transition region lines of Si III and O IV, respectively, although for O IV, the four independent ratios gave values of $\log P_e$ between 15.28 ± 0.08 and 16.16 ± 0.17 . The overall mean value of $\log P_e = 15.68$ was consistent with the lower and upper limits provided by lines of C III, O V and Fe XII.

We have re-examined all the pressures derived using CHIANTI (v5.2), since some changes were made following the discussions in Jordan et al. (2001b). There have been no changes to the data for the lines of C III and Si III. The pressures found from the ratios involving the O IV 1401-Å line are now slightly lower ($\log P_e = 16.01 \pm 0.17$ and 15.98 ± 0.20), but the discordant low pressures derived from ratios involving the blended line at 1404 Å are unchanged, and there are still problems with the lines of Si IV. A pressure can now be found from the lines of O V at 1218 Å and 1371 Å, and is $\log P_e = 15.95_{-0.24}^{+0.18}$. If the pressures from the ratios involving the O IV 1401-Å line are preferred, then the mean electron pressure at around $\log T_e = 5.3$ becomes $\simeq 15.97 \pm 0.2$. It should be noted that if material at pressures up to about $\log P_e = 16.30$ were present, this could be detected from the line flux ratios used.

In models of the chromosphere and transition region by Sim & Jordan (2005), a turbulent pressure term derived from the observed non-thermal line widths (Jordan et al. 2001b) is included in the equation of hydrostatic equilibrium. This results in small *increases* in P_e with increasing T_e above 3×10^4 K, where the Si III lines are formed. The pressures now derived from the transition region lines are consistent with this behaviour, to within the uncertainties given above. In our theoretical models of the upper transition region and inner corona (and in those by Sim & Jordan 2003a), P_e continues to rise by a few per cent until $\log T_e \simeq 5.8$ (see Section 6). Only a small difference in P_e is expected between $\log T_e = 5.3$ and 6.3, where the lines of O VII are mainly formed.

In the X-ray spectra, the ratio of the fluxes in the forbidden line (f) ($1s2s\ ^3S - 1s^2\ ^1S$) and the intersystem line (i) ($1s2p\ ^3P_{1,2} - 1s^2\ ^1S$) in the He I-like ions is potentially sensitive to n_e (Gabriel & Jordan 1969). Of the He I-like ions observed with the LETGS, only O VII has lines that are sufficiently strong and unblended to use in a measurement of n_e . Because of the importance of the measured flux ratio we have varied the continuum level and line widths used in extracting the fluxes, in order to obtain realistic error bars. The spectrum and these fits are shown in Fig. 1. The mean observed ratio is $2.88_{-0.34}^{+0.57}$. Provided the same widths are used for both lines, uncertainties in the widths have less effect than those in the choice of continuum. The range of the observed ratio is 2.535 – 3.455, compatible with the ratio of 3.06 measured by Sanz-Forcada et al. (2004), who allowed explicitly for contributions from what they regarded as weak unidentified lines.

Using CHIANTI (v4.2), at $T_e = 2 \times 10^6$ K, the observed

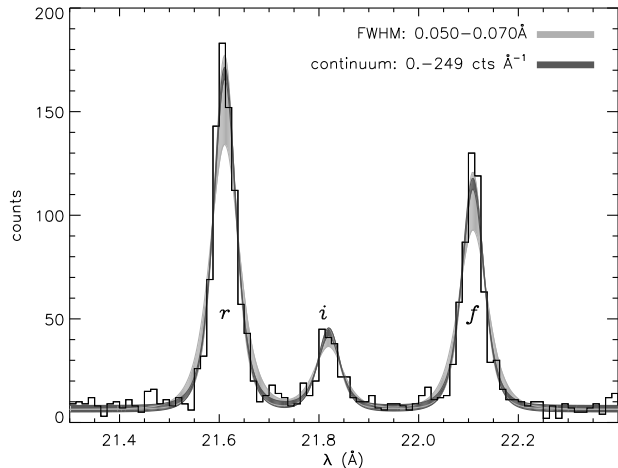


Figure 1. The spectral region including the O VII triplet. The light grey shade indicates the best fits when the background is fixed at 10 counts \AA^{-1} and the line width is varied between values of 0.050 \AA – 0.070 \AA . The dark grey shade indicates the best fits when the line width is fixed at 0.053 \AA and the background is varied between values of 0 – 249 counts \AA^{-1} .

ratio of 2.88 leads to $\log P_e = 16.35$, with a range of 16.54 – 16.00. The lower limit is consistent with the pressure found from the transition region lines at $\log T_e = 5.3$. This pressure is essentially the same as the value of $\log P_e = 16.33$ found in an earlier analysis by Ness et al. (2002), which was adopted by Sanz-Forcada et al. (2004). (Using atomic data from APED gives essentially the same results.) CHIANTI (v4.2) predicts a ratio of 3.9 in the low-density limit, but does not include recombination to the $n = 2$ levels, either directly or via cascades. Early work by Gabriel & Jordan (1973) showed that including both radiative and di-electronic recombination tends to increase the predicted ratio in the low-density limit, but by only a relatively small amount; collisional excitation followed by cascades is more important. They predicted a low-density limit of 3.64. Blumenthal et al. (1972) found larger effects from recombination, but according to Gabriel & Jordan (1973) they overestimated the contributions from di-electronic recombination.

The most recent version of CHIANTI (v5.2) gives the option of including radiative recombination as a process populating the excited states. The implementation of radiative recombination in CHIANTI (v5.2) is not correct, since it does not take into account recombination to the $1s2p$ 3P_0 level (Landi et al. 2006) and hence omits an important process for populating the $1s2s$ 3S level. This leads to lower values of the f/i ratio at a given value of n_e . In particular, the value of f/i at low densities (R_o) becomes $\simeq 3.35$.

Porquet & Dubau (2000) have given radiative and di-electronic recombination rate coefficients and effective collision strengths for populating the $n = 2$ levels, including the effects of cascades from $n > 2$ in all cases. At $\log T_e = 6.3$ their calculations predict a value of $R_o = 3.82$, a little smaller than that found from CHIANTI (v4.2). Compared with the work by Gabriel & Jordan (1973), Porquet & Dubau (2000) find larger contributions from collisional excitations, followed by cascades, to levels with $n > 2$. Using the calculations by Porquet & Dubau (2000) (but neglecting the small contribution from recombination,

since this causes only a small increase in R_o) leads to pressures that are similar to those from CHIANTI (v4.2) ($\log P_e = 16.38$, with a range from 16.56 to 15.93). Here the lower limit is compatible with the pressure found at around $\log T_e = 5.3$, without considering the error bars.

At present, the origin of the higher optimum pressure found from the O VII lines is not clear, but we think that it is in part due to remaining uncertainties in the atomic data, as well as those in the flux measurements. A fuller atomic model for the He I-like ions is clearly needed in CHIANTI. Ideally, the value of R_o should be established from observations of the *quiet* solar corona, where the density is expected to be sufficiently low to give this limiting ratio. Gabriel & Jordan (1973) used an observed ratio of 3.6 in this manner, although Blumenthal et al. (1972) quote higher ratios of 3.78 and 3.92. Unfortunately, the LETGS spectra of α Cen A (Ness et al. 2002), where a solar-like pressure might be expected, do not have sufficient flux in the O VII lines to measure R_o to within useful limits.

The EUVE lines of Fe XIV are formed around $\log T_e = 6.25$, within the range over which the O VII lines are formed. Laming et al. (1996) found $\log P_e = 15.25$ from the lines at 211.33 \AA and 219 \AA , but the latter is weak and blended. Using the 211.33- \AA and 264.78- \AA lines, Schmitt et al. (1996) found $\log P_e = 15.55$, still lower than that indicated by the O VII and transition region lines.

A number of other line ratios are sensitive to n_e , because the relative populations of the levels in the ground term are not given by the Boltzmann population (e.g. lines in the B I-like isoelectronic sequence and lines of iron). The densities derived depend on the overall form of the EMD and relative element abundances and are discussed in Section 4.5 and Section 4.6.1.

In the calculations that follow in Sections 4 and 5 we have explored the results using pressures of $\log P_e = 15.30$, 15.68 and 16.10. In Section 6 we require the theoretical models to produce a value of $\log P_e = 15.97 \pm 0.20$ at $\log T_e = 5.3$.

4 EMISSION MEASURE LOCI AND LINE IDENTIFICATIONS

The identifications of the strong lines in the LETGS range are well known. In identifying other lines, and to check for blends, we used both APED (ATOMDB v1.3.1) and the CHIANTI database (v5.2) (Landi et al. 2006) to explore which transitions might be present at a given wavelength. Emission measure loci (EMLs) were then calculated for possible candidates, including any dependence on P_e .

For a spherically symmetric atmosphere, the line flux observed at the Earth is given by

$$F_{21} = \frac{R_*^2}{d^2} \frac{hc}{\lambda} \frac{n_E}{n_H} \int \frac{n_2}{n_{ion}} \frac{A_{21}}{n_e} \frac{n_{ion}}{n_E} G(r) f(r) n_e n_H dr \quad (1)$$

where $G(r)$ is the fraction of photons not intercepted by the star, $f(r) = r^2/R_*^2$ and d is the distance to the star. The excited and lower levels are 2 and 1, respectively (where 1 is not necessarily the ground state); n_E/n_H is the abundance of the element relative to hydrogen, taken as constant over the region of line formation; n_{ion}/n_E is the relative ion population; n_H is the hydrogen number density; A_{21} is

the spontaneous transition probability and the integration is over the radial distance, dr .

Equation (1) can be rewritten as

$$F_{21} \simeq g(n_e, T_e) \int n_e n_H G(r) f(r) dr \quad (2)$$

where $g(n_e, T_e)$ includes all other terms in equation (1). Provided any dependence on P_e is taken into account, the emission measure locus (EML) gives the value of the *apparent* emission measure ($EM = \int n_e n_H G(r) f(r) dr$) that would be required to account for all the observed flux, at each value of T_e in turn. The loci therefore provide useful constraints on the mean EMD, since if this exceeds the minimum of a locus by more than a small factor, too much flux will be predicted when the mean EMD is used to predict the line fluxes.

It is important to note that loci from lines of different isoelectronic sequences can have different variations of $g(T_e)$ with T_e , owing to the systematic differences in n_{ion}/n_E as a function of T_e . Otherwise, if a line with a broad $g(T_e)$ function were compared with one with a narrow $g(T_e)$ function, an incorrect relative element abundance would be deduced. These differences are taken into account in finding the mean EMD (see Section 5).

Values of $n_2 A_{21}/n_e$ have been calculated using CHIANTI (v5.2). The relative ion populations for iron have been taken from Arnaud & Raymond (1992). For O VI, the calculations given in Sim & Jordan (2005) have been adopted, since these include the density dependence of dielectronic recombination. All other values are taken from Arnaud & Rothenflug (1985). The element abundances initially adopted and the corrections to these required by the observations are discussed in Section 5.

The lines of elements other than iron are now discussed according to their isoelectronic sequence. Comparisons have been made between observed and predicted line flux ratios (or relative EMLs) using a single temperature for the line formation and also using the total fluxes predicted using the final EMD. Unless otherwise stated, both approaches give the same results. Although only the lines that we regard as the most reliable are used to determine the mean EMD, we calculate the predicted fluxes in all the lines discussed below and later compare these with the observed fluxes.

4.1 Hydrogen-like lines

The (unresolved) Lyman α lines of C VI, N VII, O VIII, Ne X and Mg XII are all observed, although the Mg XII lines are weak. The Ne X lines at 12.13 + 12.14 Å are blended with a line of Fe XVII at 12.12 Å. Another line of Fe XVII is observed at 12.27 Å. The ratio of these two Fe XVII lines does not depend significantly on T_e so we have used the line at 12.27 Å to predict the flux in the line at 12.12 Å. This results in 73 per cent of the observed total flux in the line at 12.13 Å being due to Ne X.

The Lyman β lines are observed in O VIII (at 16.01 Å) and Ne X (at 10.23 Å), but the former is blended with a line of Fe XVIII at 16.00 Å. Another line of Fe XVIII at 16.07 Å has been used to find the contribution of the 16.00-Å line to the total flux. The ratio of the Fe XVIII lines is slightly sensitive to T_e , and their temperature of optimum formation could lie between $\log T_e = 6.5$ and 6.8. The total predicted fluxes

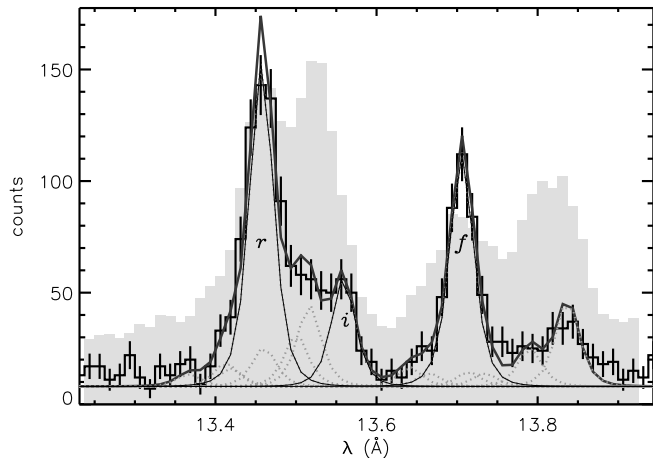


Figure 2. The spectral region around the Ne IX triplet in ϵ Eri and Capella (light grey shade), rescaled to match the peak flux in the r line. The contributions from the lines of Fe XVII, XVIII and XIX in ϵ Eri are shown by dotted lines. Those for the r, i and f lines are shown by full lines. The blending in ϵ Eri is clearly far less severe than in Capella. The method of fitting is described in the text. The fluxes derived for the Ne IX lines, and their uncertainties, are given in Table 3.

show that 81 per cent of the observed line at 16.01 Å is due to O VIII. The ratio of the observed flux in O VIII Lyman β to that in the Lyman α line is then a factor of 1.2 larger than that predicted using the mean EMD. In Ne X, the observed Lyman β to Lyman α ratio is a factor of 1.4 larger than predicted.

4.2 Helium-like lines

The resonance (r), intersystem (i) and forbidden line (f) of C V lie in a region of low and rapidly varying effective area and a real signal is observed only in the r line at 40.27 Å. However, this is slightly blended with the third order of the Ne IX r-line and it is hard to determine a reliable flux (Ness et al. 2001). The uncertainty in the flux given in Table 3 includes the results of varying the background and line width. The r-line of N VI is present, although rather weak; the i and f-lines are not sufficiently above the local noise level to be useful. The lines of O VII are relatively strong and their use in constraining P_e has been discussed in Section 3. Note that the contribution from radiative recombination has been included when predicting the fluxes in the singlet lines of all the He I-like ions.

The lines of Ne IX are also relatively strong, but are blended to various degrees with lines of Fe XVII, XVIII and XIX. A comparison between the LETGS spectra of ϵ Eri and Capella, shown in Fig. 2, indicates that the blends with lines of iron are less important than in Capella. In ϵ Eri, the Fe XVII line at 13.83 Å is significantly weaker than the Ne IX f line and the Fe XIX + XXI blend at 13.51 Å is significantly weaker than the r line. The de-blending problem is therefore less severe than in Capella. The procedure used is as follows: the amplitudes and wavelengths of the lines observed in Capella using the High Energy Transmission Grating Spectrograph (HETGS) (see Ness et al. 2003a) are used to predict the counts in the LETGS spectra, taking into

account the resolution and effective area of the LETGS; the lines of Fe XVII and Fe XVIII are grouped together, as are the lines of Fe XIX, while the lines of Ne IX are treated individually; the amplitudes of the 2 groups and 3 individual lines are scaled iteratively to obtain the best fit to the LETGS spectrum of ϵ Eri and hence the fluxes in the Ne IX lines are determined. The fits made are shown in Fig. 2. The analyses of all lines of neon and other lines of iron shows that the relative weakness of the blended iron lines in ϵ Eri arises from both the lower EMD above $\log T_e = 6.6$ and a lower Fe/Ne relative abundance. Given the de-blending process, in particular for the i-line, it is difficult to make a reliable interpretation of the relative fluxes in the Ne IX r, i and f lines.

The r and f lines are present in Mg XI and Si XIII, but the i lines cannot be distinguished. In extracting fluxes we have summed over the r, i and f lines. The predicted fluxes are lower limits, since the contribution to the populations of excited states from dielectronic recombination is not yet included in CHIANTI (v5.2), and contributions from satellite lines are not yet included for Mg XI.

The $1s3p\ ^1P - 1s^2\ ^1S$ transition in O VII is present as a weak line at 18.63 Å, but is blended with a weaker line. The same transition in Ne IX might also be present at 11.54 Å. These weak lines are not used in deriving the mean EMD.

4.3 Lithium-like lines

In the region below 170 Å the transitions observed in the Li I-like ions are those between the $n = 3$ and $n = 2$ levels ($3p - 2s$, $3d - 2p$, $3s - 2p$). The $3p - 2s$ (unresolved) lines in O VI at 150.1 Å are present in the minus direction spectrum, but are barely above the instrumental noise level in the plus direction spectrum. The measured flux is very sensitive to the background adopted and provides only an upper limit to the EML. Although the $3p - 2s$ lines are not included in the derivation of the mean EMD, this reproduces the observed flux to within a factor of 1.1. The $2p - 2s$ transitions are both observed (around 1032 Å and 1038 Å) in spectra obtained with FUSE in 2000 December. They are useful in constraining the EMD between $\log T_e = 5.5$ and 6.1 (see Section 5).

In Ne VIII the $3p - 2s$ and $3d - 2p$ transitions are observed at around 88.1 Å and 98.2 Å, respectively. Although the $3s - 2p$ transitions are just present around 103.1 Å, they are too weak to yield a reliable flux. The $4d - 2p$ transitions occur around 73.5 Å but on the basis of the calculated EMLs, the line observed is identified as one of Fe XV. Heroux et al. (1972) suggested that in the solar spectrum, the lines around 88.1 Å are blended with lines of Fe XI and identify a line at 86.88 Å with the strongest member of the multiplet (at solar densities). At the higher value of n_e in ϵ Eri, the line at 86.88 Å should still be the strongest member of the multiplet, but is not observed. We have rejected the possibility of a second order line of Si XII at 88.04 Å because a stronger second order Si XII line at 88.34 Å is not present. Thus significant blending with these Ne VIII lines seems unlikely. Note that the relevant lines of Fe XI are not yet included in either CHIANTI or APED. Heroux et al. (1972) also suggested that both of the lines at 98.11 Å and 98.26 Å are blended with other lines in the solar spectrum. In ϵ Eri, to within the measurement uncertainties, the two

lines have the expected wavelength separation and almost the theoretical flux ratio, so there is no obvious evidence of substantial blending.

The lines in Mg X are all weak. The $3p - 2s$ multiplet at 57.90 Å is not resolved; only the summed flux is used. The $3d - 2p$ transitions at 63.30 Å + 63.31 Å and 63.16 Å are observed only in the minus direction spectrum, owing to a chip gap in the plus direction. We use only the blend of transitions at around 63.3 Å in deriving the EMD, since the weaker line at 63.16 Å is barely above the noise level. The $3s - 2p$ lines at 65.67 Å and 65.85 Å have an incorrect flux ratio in the minus side spectrum and summed spectra, suggesting that the intrinsically weaker line at 65.67 Å is blended. Also, the line at 65.85 Å might be blended with another line at around 65.93 Å making it difficult to extract a reliable flux; these two Mg X lines are excluded from the derivation of the mean EMD.

In Si XII the $3p - 2s$ lines lie around 40.93 Å in the region of the instrumental absorption edge, and are not observable. The $3d - 2p$ transitions at 44.02 Å and 44.17 Å are observed as moderately strong lines. The observed ratio of the stronger to weaker components is about 1.5, instead of the predicted value of 1.99. We use only the stronger line, on the grounds that the weaker line might be blended. The $3s - 2p$ lines at 45.52 Å and 45.69 Å are also observed, but are not used in deriving the mean EMD, as they are weak and blended with other weak lines or instrumental noise.

There are weak lines that are possibly due to S XIV. A line at 32.56 Å corresponds to the stronger component of the $3d - 2p$ transitions. Another at 30.46 Å corresponds to the $3p - 2s$ transitions, but the $2p^5 3d\ ^1P - 2p^6\ ^1S$ transition in Ca XI occurs at 30.47 Å and could contribute to the measured flux. These lines were not used in deriving the mean EMD.

In Ne VIII the ratio of the observed flux from the $3p - 2s$ transitions to that in the $3d - 2p$ transitions is about a factor of 1.5 larger than predicted. This suggests that the atomic models or atomic data for the lithium-like ions would bear closer examination.

4.4 Beryllium-like lines

No lines of Mg IX are observed. Because it is useful to constrain the EMD at around 10^6 K, we have used the background level at 72.31 Å and 77.74 Å (the wavelengths of the $2s3d - 2s2p$ and $2s3s - 2s2p$ transitions, respectively), to find the upper limit to their EMLs.

Three singlet lines of Si XI are observed; the $2s3p - 2s^2$ line at 43.76 Å, the $2s3d - 2s2p$ line at 49.22 Å and the $2s3s - 2s2p$ line at 52.30 Å (but the latter only in the plus side spectrum). Only the 52.30-Å line appears to be unblended.

The strongest transition ($2s3d - 2s2p$) in S XIII is observed at 35.67 Å; other transitions are present, but are barely above the noise level.

4.5 Boron-like lines

The $3d - 2p$ lines of Si X lie at 50.69 Å ($^2P_{3/2} - ^2D_{5/2,3/2}$) and 50.52 Å ($^2P_{1/2} - ^2D_{3/2}$). As in Fe XIV (Jordan 1965), the ratio of these lines depends on n_e , since the relative populations of the ground 2P levels have a Boltzmann distribution only at large values of n_e . The line at 50.52 Å

is blended with a line of Fe xvi at 50.55 Å and careful deblending is required. Using the procedure described in Section 4.6.3, the ratio of the deblended fluxes in the 50.69 and 50.52-Å lines is 1.52 ± 0.26 . Using CHIANTI (v5.2) and the mean EMD, the predicted integrated fluxes give ratios of 1.51 at $\log P_e = 15.68$, 1.18 at $\log P_e = 15.30$ and 1.78 at $\log P_e = 16.10$. Thus a value of $\log P_e$ close to 15.68 gives the best fit, but the uncertainty in the flux ratio just includes $\log P_e = 16.10$. The flux in the unblended Si x line at 50.69 Å is also weakly dependent on n_e (compared with the n_e^2 dependence of most lines). At $\log P_e = 15.68$, the flux predicted by CHIANTI (v5.2) is a factor of 1.3 larger than that observed and a pressure of $\log P_e \leq 15.30$ would be required to fit the observed flux. Predicted flux ratios are in general more accurate than absolute fluxes, since they do not depend on abundances or ion fractions, so there may be small problems with the atomic data.

The corresponding lines of S xii are not observed.

4.6 Lines from iron ions

We now discuss the lines of iron according to their stage of ionization.

4.6.1 Fe ix to Fe xiv

For these ions we rely on the $\Delta n = 0$ transitions observed with the *EUVE*, although the Fe ix line is also observed with the LETGS. We also discuss the Fe xii forbidden lines that are observed with the STIS. At present, neither CHIANTI (v5.2) nor APED include all transitions of the type $\Delta n = 1$ in these ions. We have updated earlier calculations of the EMLs by using CHIANTI (v5.2) (including those by Sim & Jordan 2003a, who used CHIANTI v4).

The lines of Fe ix to xiv used are *all* sensitive to n_e , either through the departure from Boltzmann populations in the levels of the ground term, or from the population of higher metastable states. Apart from the blended lines of Fe xiii at 203.83 Å the derived EMLs all increase with increasing n_e . The stronger 203.83-Å line ends on an excited level of the ground term and thus has the opposite behaviour. To give a smoothly increasing EMD from all the lines of Fe x to xv would require a value of $\log P_e \leq 15.30$; at higher pressures the Fe xiii locus lies below the mean value. Since there is no other evidence of such a low pressure, there might be small problems with the atomic data for Fe xiii in CHIANTI (v5.2) or in the *EUVE* line fluxes. With the inclusion of more levels in the atomic models of these ions, it might be possible to derive a value of P_e .

The resonance line of Fe ix at 171.07 Å leads to a relatively low EML, irrespective of pressures in the range from $\log P_e = 15.3$ to 16.1. Even at $\log P_e = 16.10$, the mean EMD leads to a flux that is larger than the value observed with the *EUVE* by a factor of 1.8. The 171-Å line falls near the long wavelength limit of the LETGS and the short wavelength limit of the *EUVE* medium wavelength spectra; for both instruments there are significant uncertainties in the flux calibration at 171 Å and these could be one origin of the above discrepancy. As discussed by Laming et al. (1996), the ion balance calculations by Arnaud & Rothenflug (1985) lead to a larger EML than that found from the calculations

by Arnaud & Raymond (1992). Near the peak emissivity, the difference between these calculations is a factor of 1.6, which would remove much of the discrepancy. However, the calculations by Arnaud & Raymond (1992) are expected to be more accurate. The final model can be used to estimate the line centre opacity. This is close to 1; although scattering of photons out of the line of sight could occur, detailed radiative transfer calculations are needed to find the effect on the spatially integrated line fluxes.

The atomic data for Fe xii have been revised since the work by Jordan et al. (2001a,b), who used CHIANTI (v3.01), and by Sim & Jordan (2003a), who used CHIANTI (v4.2). We have therefore re-examined the difference between the fluxes predicted by CHIANTI (v5.2) for the forbidden lines at 1242 and 1349 Å and the *EUVE* lines in the blend around 196 Å. For the lines at 1242 Å and at around 195 Å, Jordan et al. (2001a) found a difference of a factor of 3 between their EMLs. This is now reduced to a factor of 1.8 (at $\log P_e = 15.68$) or 2.2 and 1.5 (at $\log P_e = 15.30$ and 16.10, respectively). The small dependence on P_e arises from a small increase in the forbidden line fluxes, and a small decrease in the EUV line fluxes, with increasing P_e . Using the absolute line fluxes and the mean EMD, the agreement between the observed and predicted fluxes for the EUV lines is very good (to within a factor of 1.1 over the above range of P_e) but the flux in the line at 1242 Å is predicted to be smaller than that observed, by the factors given above. Although differences in the fluxes arising from the different dates of the observations cannot be ruled out, neither can small corrections to the level populations for the forbidden lines (see below).

The ratio of the fluxes in the Fe xii forbidden lines at 1242 Å and 1349 Å is insensitive to $\log P_e$ over the range from about 15.0 to 16.0, but is useful in placing an upper limit on P_e . In ϵ Eri the observed ratio is 1.88 (± 0.2) (and other main-sequence stars show a similar ratio) (Jordan et al. 2001a). Using a single temperature of $\log T_e = 6.15$, CHIANTI (v3.01) leads to $\log P_e = 15.72$, with an upper limit of 16.17. CHIANTI (v4.2) leads to $\log P_e = 15.53$, with an upper limit of 16.07. But CHIANTI (v5.2) leads to a pressure of $\log P_e = 14.21$, which is much lower than the transition region pressure found in Section 3. The upper limit is 15.80, which is consistent with the transition region pressure (15.97 ± 0.20), but not with the pressure of $\log P_e = 16.14$ found in the final model at $\log T_e = 6.15$. At present we suggest that the atomic data used in CHIANTI (v3.01) or (v4.2) give a better fit to the forbidden line flux ratio than do those in CHIANTI (v5.2) (see Storey et al. 2005).

The value of the Fe xii forbidden line flux ratio provides a very sensitive test of the atomic data for these lines. E.g. Jordan et al. (2001b) pointed out that the ratio of 2.7 predicted by Binello et al. (2001) could not be correct. It is also of interest to compare the population of the $3p^3 \ ^2P_{1/2}$ level from CHIANTI (v5.2) with that predicted empirically by Gabriel & Jordan (1975) on the basis of solar observations. At $T_e = 1.65 \times 10^6$ K and $n_e = 3 \times 10^8$ cm $^{-3}$, CHIANTI (v5.2) gives a level population (relative to that of the ion) of 2.9×10^{-4} , whereas the solar observations led to values between 3.3 and 5.1×10^{-4} . Thus there is other observational support for a larger $^2P_{1/2}$ population.

Given that the final EMD peaks around the tempera-

ture where Fe XV and XVI are formed, one might expect lines of Fe XIV to be present in the X-ray region. There are four weak lines around 76 Å that are also present in the LETGS spectra of Procyon (Raassen et al. 2002), α Cen A and B (Raassen et al. 2003) and Capella (Sanz-Forcada et al. 2004). In ϵ Eri the lines are at 75.91 Å, 76.04 Å, 76.13 Å and 76.53 Å. We propose that the lines at 76.04 Å and 76.13 Å are due to the $3d^2D - 4f^2F$ transitions in Fe XIV, but owing to the absence of these lines in CHIANTI or APED we cannot check this through derived EMLs. Raassen et al. (2003) have also proposed this identification for lines in α Cen A and B. In Procyon, a line at 75.98 Å may well be due to Fe X (Raassen et al. 2002), but in ϵ Eri the EMD is relatively smaller where such lines are formed. Using our final EMD, none of the four possible lines of Fe XIV between 75.69 Å and 76.82 Å are predicted to be observable. A line of Fe XVI occurs at 76.50 Å but the next strongest member of the multiplet at 76.80 Å is absent (see also Section 4.6.3).

4.6.2 Fe XV

The resonance line at 284.2 Å is observed as a strong line with the *EUVE*. Using our final EMD, the flux predicted in this line is a factor of 1.16 larger than that observed. Possible sources of uncertainty include the amount of absorption by the ISM and line opacity effects.

The X-ray spectrum of Fe XV in a solar flare and Capella has been discussed by Keenan et al. (2006) and we make comparisons with predicted flux ratios at $\log T_e = 6.3$ (near where the EMLs for the Fe XV lines have their minimum value) and $\log T_e = 6.5$ (to allow for the increase in the mean EMD). We also make comparisons with the flux ratios predicted using CHIANTI (v5.2) and the mean EMD. We observe only singlet transitions whose flux ratios do not depend on n_e .

The $3s4d^1D - 3s3p^1P$ (59.40 Å) transition is adopted as the standard line. The blend at 59.27 Å observed in Capella by Keenan et al. (2006) is not obvious in ϵ Eri, consistent with their suggestion that it is due to Fe XVII. The 59.40-Å line flux is a factor of 1.38 larger than that predicted using CHIANTI (v5.2) and the mean EMD.

The $3s4p^1P - 3s^2^1S$ transition at 52.91 Å is not obviously blended in ϵ Eri, unlike the situation in Capella. The observed flux ratio agrees well with that predicted using CHIANTI (v5.2), and although the flux ratio from Keenan et al. (2006) is smaller, it also agrees with that observed to within the uncertainties.

The strongest X-ray line is both predicted and observed to be the $3s4s^1S - 3s3p^1P$ transition at 69.68 Å. In ϵ Eri this line is blended with one at around 69.6 Å that does not appear to be present in Capella ((Keenan et al. 2006)). We note that Kelly (1987) lists predicted lines of Fe XIV in this region. The flux ratio observed for the line at 69.68 Å is a factor of about 1.5 lower than that predicted by both CHIANTI (v5.2) and Keenan et al. (2006), which agree well with each other. This ratio is also lower than expected in Capella, but agrees with the theoretical value to within the uncertainties.

The $3s4f^1F - 3s3d^1D$ transition occurs at 73.47 Å, but is potentially blended with a line of Ne VIII at 73.48 Å. Interpreting the observed line flux as being due entirely to Ne VIII, using CHIANTI and the mean EMD gives an ob-

Table 5. Fe XV line flux ratios, relative to the flux in the 59.40-Å line^a.

| Line (Å) | Keenan et al. (2006) | CHIANTI (v5.2) ^b | Observed |
|----------|----------------------|-----------------------------|-------------------|
| | $\log T_e$ | | |
| 52.91 | 6.3 0.65 ± 0.13 | 0.81 | 0.75 ± 0.17 |
| | 6.5 0.64 ± 0.13 | | |
| 69.68 | 6.3 3.1 ± 0.6 | 2.75 | 1.85 ± 0.31 |
| | 6.5 2.7 ± 0.5 | | |
| 73.47 | 6.3 0.97 ± 0.16 | 1.01 | 0.68 ± 0.20^c |
| | 6.5 0.75 ± 0.12 | | 0.91 ± 0.22^d |
| 284.2 | | 56.0 | 34.8 ± 5.6 |

^a This is $2.99 \pm 0.44 \times 10^{-14}$ erg cm⁻² s⁻¹, when corrected for absorption in the ISM.

^b Predicted using the mean EMD (see Table 10), using $\log P_e = 16.10$.

^c With the predicted contribution from Ne VIII removed.

^d Assuming no contribution from Ne VIII.

served to predicted flux ratio that is a factor of 4.0 too large. Assuming that the predicted Ne VIII flux is correct, its contribution can be removed to give an Fe XV flux of 2.04×10^{-14} erg cm⁻² s⁻¹ and a flux ratio of 0.68. The temperature sensitivity of the Fe XV 73.47-Å line is not given by Keenan et al. (2006) so that of the triplet lines from the same configuration has been used to find the expected flux ratio at $\log T_e = 6.50$. This corrected flux ratio agrees well with the flux ratio predicted by Keenan et al. (2006), but the flux ratio predicted using CHIANTI is larger. However, the stronger member of the Ne VIII multiplet that should occur at 73.56 Å is not present with the flux expected from CHIANTI. For this reason we have also found the observed flux ratio assuming no contribution from Ne VIII, and this agrees with that predicted using CHIANTI, to within the uncertainty.

The predicted and observed flux ratios are summarized in Table 5. We have checked that the uncertainties in the observed ratios also cover the range of values derived using a range of background levels. Of the X-ray lines, only the observed flux ratio for the line at 69.68 Å is discordant with the calculations. On average, the flux ratios predicted by Keenan et al. (2006) are smaller than those predicted using CHIANTI (v5.2).

At present, the atomic model does not include levels with n larger than 5; this could be one cause of the remaining differences between the observed and calculated flux ratios for transitions from the $n = 4$ levels. Also, from section 2.3 of Landi et al. (2006), the effects of recombination and ionization on the populations of excited states have not yet been included for Fe XV.

4.6.3 Fe XVI

In addition to the $3p - 3s$ transitions observed with the *EUVE*, lines from the $4p - 3s$, $4d - 3p$, $4s - 3p$ and $4f - 3d$ transitions are observed in the LETGS spectrum. Thus it is possible to test the atomic data used in CHIANTI (v5.2); these were not updated from those used in CHIANTI (v4.2).

To make comparisons between the observations and the theoretical values from Cornille et al. (1997) and CHIANTI (v5.2), we use the $4s - 3p$ line at 63.72 Å as the standard

Table 6. Fe XVI line flux ratios, relative to the flux in the 63.72-Å line^a.

| Line (Å) | Cornille et al. (1997) | CHIANTI (v5.2) ^b | Observed |
|------------------|------------------------|-----------------------------|------------------------------|
| $\log T_e = 6.5$ | | | |
| 50.35 | 0.33 | 0.23 | 0.57 ± 0.08 |
| 50.55 | 0.17 | 0.13 | 0.31 ± 0.04 |
| 54.14 | 0.29 | 0.21 | 0.46 ± 0.07 |
| 54.74 | 0.57 | 0.41 | 0.77 ± 0.10 |
| 62.87 | 0.49 | 0.49 | 0.44 ± 0.08 |
| 66.26 | 0.41 | 0.34 | 0.61 ± 0.10 ^c |
| 66.37 | 0.58 | 0.51 | 0.95 ± 0.13 ^c |
| 335.4 | | 14 | 14 ± 2 |
| 360.8 | | 6.9 | 7.3 ± 1.0 |

^a This is $6.25 \pm 0.57 \times 10^{-14}$ erg cm⁻² s⁻¹, when corrected for absorption by the ISM.

^b Predicted using the mean EMD (see Table 10), using $\log P_e = 16.10$.

^c With no correction for the upper limit to the contribution from the 3rd order O VII 22.10-Å line.

line. Using CHIANTI (v5.2) and the integrated fluxes, the predicted and observed ratios of this and the lines at 335 Å and 361 Å agree to within 7 per cent.

The 4p – 3s transitions at 50.35 and 50.55 Å are blended with the third-order of the Fe XVII line at 16.78 Å and with the density-sensitive line of Si X at 50.52 Å. The plus-side spectrum was used to carry out the deblending, because the effective area varies rapidly in the minus-side spectrum. The fluxes in the third-order lines of Fe XVII at 17.05 and 17.10 Å have been measured and the ratio of the fluxes in these lines to that at 16.78 Å have been found from the first-order spectrum. Using integrated fluxes it is found that the Fe XVI line at 50.35 Å contributes 71 per cent of the observed flux. At $\log T_e = 6.5$, the theoretical ratio of the Fe XVI lines at 50.35 and 50.55 Å is 1.93, from Cornille et al. (1997) or 1.82, from CHIANTI (v5.2), using integrated fluxes. Hence, using CHIANTI (v5.2), Fe XVI contributes 51 per cent of the line at 50.54 Å. The discrepancy between the flux ratio for the 50.35-Å line is then a factor of 1.7, using Cornille et al. (1997), or 2.5, using CHIANTI (v5.2). These factors are significantly larger than the average found from other lines and these lines are not used in finding the mean EMD.

The 4d – 3p lines at 54.72 + 54.76 and 54.14 Å are observed only in the plus-side spectra, but are relatively strong, clean lines. Using the calculations by Cornille et al. (1997), the flux ratio for the blended lines at $\simeq 54.74$ Å is a factor of 1.3 smaller than that observed. Using CHIANTI (v5.2), at the same T_e or using integrated fluxes, the predicted flux ratio is a factor of 1.9 smaller than that observed.

The 4f – 3d transitions occur at 66.37 and 66.26 Å. The observed ratios of the fluxes in these lines to that of the 63.72-Å line are larger than those predicted by either CHIANTI (v5.2) (using the mean EMD) or Cornille et al. (1997), but the flux ratios using the latter are closer to those observed. The third order line of O VII at 22.10 Å occurs between these lines, but, on the basis of the upper limit to the flux in the O VII line at 21.60 Å, the contribution from the 22.10-Å should be very small and its inclusion would not remove the above discrepancy.

The 4p – 3d transitions around 76.5 Å have smaller

branching ratios than the 4p – 3s transitions. If the weak line at 76.53 Å is interpreted as being due to Fe XVI, then the observed flux is about a factor of 5 larger than that predicted by CHIANTI (v5.2). (Cornille et al. 1997) do not give theoretical relative intensities for the 4p – 3d transitions. This large discrepancy rules out the identification of the line at 76.5 Å as Fe XVI, particularly since the next strongest member of the multiplet expected at 76.80 Å is not observed. The calculations of the transition probabilities by Cornille et al. (1997) and by Eissner et al. (1999) are in good agreement with each other for these transitions. (We note that the ωf value for the 4p ²P_{3/2} – 3d ²D_{3/2} transition given by Cornille et al. (1997) is a factor of 100 larger than expected from their *A*-value, and that this typographical error has been reproduced in the comparisons made by Eissner et al. 1999.)

The above comparisons are summarized in Table 6. Again, we have checked that the uncertainties in the observed fluxes cover the range of values found using different background levels.

Because we have used the line at 63.72 Å as the standard, the discrepancies would of course all be smaller if the predicted flux for this line (and for the 3p – 3s lines observed with the *EUVE*) were smaller than indicated by the given statistical uncertainties, but this is not supported by the overall behaviour of the other iron lines. The atomic model and data for Fe XVI have received close attention and the differences between the flux ratios predicted using Cornille et al. (1997) and CHIANTI (v5.2) are smaller than those between either of these sources and the observed flux ratios. Overall, the flux ratios predicted using Cornille et al. (1997) at $\log T_e = 6.50$ are slightly closer to the observed ratios than are those using CHIANTI (v5.2) and the mean EMD. Relative to the 4s – 3p and 4f – 3d transitions, the other line flux ratios do increase with T_e , but the mean EMD shows that little material exists at the very high temperatures required to bring the predicted ratios closer to those observed. Also, the lower fluxes measured for the higher ions of iron with the LETGS, compared with those measured from *EUVE* or the RGS make it unlikely that flaring was present in the LETGS spectra.

As for Fe XV, the effects of including further *n*-states and of recombination and ionization to and from excited states still need to be investigated.

4.6.4 Fe XVII

The 2p⁵3d – 2p⁶ transitions are observed at 15.01 Å and 15.26 Å and the 2p⁵3s – 2p⁶ transitions are observed at 16.78 Å and 17.05 + 17.10 Å. The predicted flux in the 15.01-Å line is only slightly too large, in spite of the fact that the lower collisional excitation rate suggested by laboratory measurements by Brown et al. (2006) has not been adopted in CHIANTI (v5.2). The line at 15.26 Å is observed to be a factor of 1.45 stronger than predicted. Without knowing n_e at high values of T_e , optical depth effects cannot be estimated. However, Brickhouse & Schmelz (2006) have suggested that an inner shell transition of Fe XVI occurs at 15.26 Å, but its contribution is not included in the predicted flux.

Table 7. Photospheric abundances relative to solar values, with their \pm uncertainties, where available.

| [C/H] | [O/H] | [Mg/H] | [Si/H] | [S/H] | [Ca/H] | [Fe/H] | [Ni/H] | Reference |
|-------|--------------|--------------|--------------|--------------|--------------|--------------|--------------|------------------------------|
| | | | -0.10 (0.05) | | -0.10 (0.07) | -0.07 | -0.16 (0.04) | Bodaghee et al. (2003) |
| | | | | | -0.10 (0.05) | -0.09 (0.05) | | Drake & Smith (1993) |
| -0.06 | -0.16 (0.02) | -0.14 (0.05) | -0.16 (0.02) | -0.01 (0.01) | -0.11 (0.03) | -0.12(0.01) | -0.20 (0.03) | Zhao et al. (2002) |
| -0.24 | -0.04 | -0.03 | -0.01 | | -0.01 | -0.06 | -0.06 | Allende Prieto et al. (2004) |

4.6.5 Fe XVIII

The resonance lines of Fe XVIII at 93.92 and 103.94 Å are observed with the *EUVE* and the LETGS, but the latter line is weak in both spectra. Since the ratio of its flux to that of the line at 93.92 Å does not agree with the theoretical value, the line at 103.94 Å is not used in determining the EMD.

Fe XVIII has many transitions of the type $\Delta n = 1$ so there are few strong lines. The optimum temperature of line formation in a uniform plasma is $\log T_e \simeq 6.8$, whereas the mean EMD peaks at around $\log T_e = 6.6$. Thus the lines of Fe XVIII are relatively weaker than in stars that have hotter coronae.

As discussed in Section 4.1, the O VIII Lyman β line at 16.01 Å is blended with a transition of Fe XVIII at 16.00 Å. The observed relative fluxes of the strongest lines at 14.21 + 14.26 Å, 16.08 Å and 93.92 Å agree with those predicted by CHIANTI (v5.2) and the mean EMD to within a factor of 1.1.

4.6.6 Fe XIX and XX

The observed lines of these ions lie between 100 and 130 Å where Sanz-Forcada et al. (2004) point out that there are suspected problems with the flux calibration. The noise levels are also large.

The line of Fe XIX at 108.36 Å is weak, and that at 101.55 Å is barely above the noise level. The EML from the line at 108.4 Å shows that the mean EMD decreases rapidly at temperatures above about $\log T_e = 6.7$. The observed ratio of these two lines (which has only a very small dependence on n_e over the range of interest) is larger than predicted, probably because of difficulty in extracting a reliable flux for the weaker line.

The decrease in the EMD at higher temperatures is confirmed by the line of Fe XX at 132.8 Å. Lines from higher ions are not definitely observed. Lines that are formed above the mean coronal temperature (allowing for the extensions of their EMLs to lower temperatures) are likely to be formed in stellar active regions, by analogy with the behaviour of the solar EMD. Since we do not have values of n_e at these high temperatures, we cannot model the active region component.

5 RELATIVE ABUNDANCES AND THE MEAN EMD

5.1 Relative photospheric abundances

The photospheric element abundances derived for ϵ Eri by Abia et al. (1988); Drake & Smith (1993); Zhao et al.

(2002); Bodaghee et al. (2003) (and references concerning Fe therein), were discussed by Sim & Jordan (2005), in the context of relative abundances in the lower transition region. All find photospheric abundances of iron that are lower than the solar value. Abia et al. (1988) used early photospheric models, and the solar abundances they derive differ significantly from recent values; their results are not considered further here. The abundances derived by the other authors, relative to solar values, are given in Table 7. These include the more recent values from Allende Prieto et al. (2004) that were adopted by Wood & Linsky (2006). Both Bodaghee et al. (2003) and Zhao et al. (2002) used LTE model atmospheres by Kurucz (1993). Bodaghee et al. (2003) used the solar abundances by Anders & Grevesse (1989) in their solar models, but Zhao et al. (2002) determined the differential abundances using their observations of the Moon, so their results have quite small uncertainties. Allende Prieto et al. (2004) also determined differential abundances using the same lines in the solar spectrum. The set of values by Zhao et al. (2002) is the most complete and we have adopted these as the initial values in deriving the EMLs, but also make comparisons with those by Allende Prieto et al. (2004). Sanz-Forcada et al. (2004) also made comparisons with the relative abundances by Zhao et al. (2002). To convert the differential photospheric abundances in ϵ Eri to absolute abundances we have used the solar photospheric abundances recommended by Asplund et al. (2005). While the solar photospheric abundances adopted affect the stellar photospheric abundances, they do not influence the relative stellar coronal abundances discussed in Section 5.3. The solar abundances recommended by Asplund et al. (2005) are based on exploratory 3-dimensional modelling and are not directly comparable with the results of the 1-dimensional stellar photospheric models. When comparing the stellar photospheric and coronal abundances in Section 5.3, we have also investigated results using solar abundances from Grevesse & Sauval (1998) that are also based on 1-dimensional modelling. Photospheric abundances are not available for nitrogen or neon. For nitrogen the mean of the carbon and oxygen differential abundances was used, whereas for neon, the solar abundance from Asplund et al. (2005) was initially adopted.

5.2 Derivation of the mean EMD

Fig. 3 shows the EMLs for lines from the H I-like, He I-like and Li I-like isoelectronic sequences (top panel), the EMLs from the lines of iron (middle panel) and all these lines (bottom panel). A value of $\log P_e = 16.10$ was adopted. These EMLs are apparent values, as defined in Section 6. Apart from the lines of Fe IX, XVI and XVII, the iron lines are

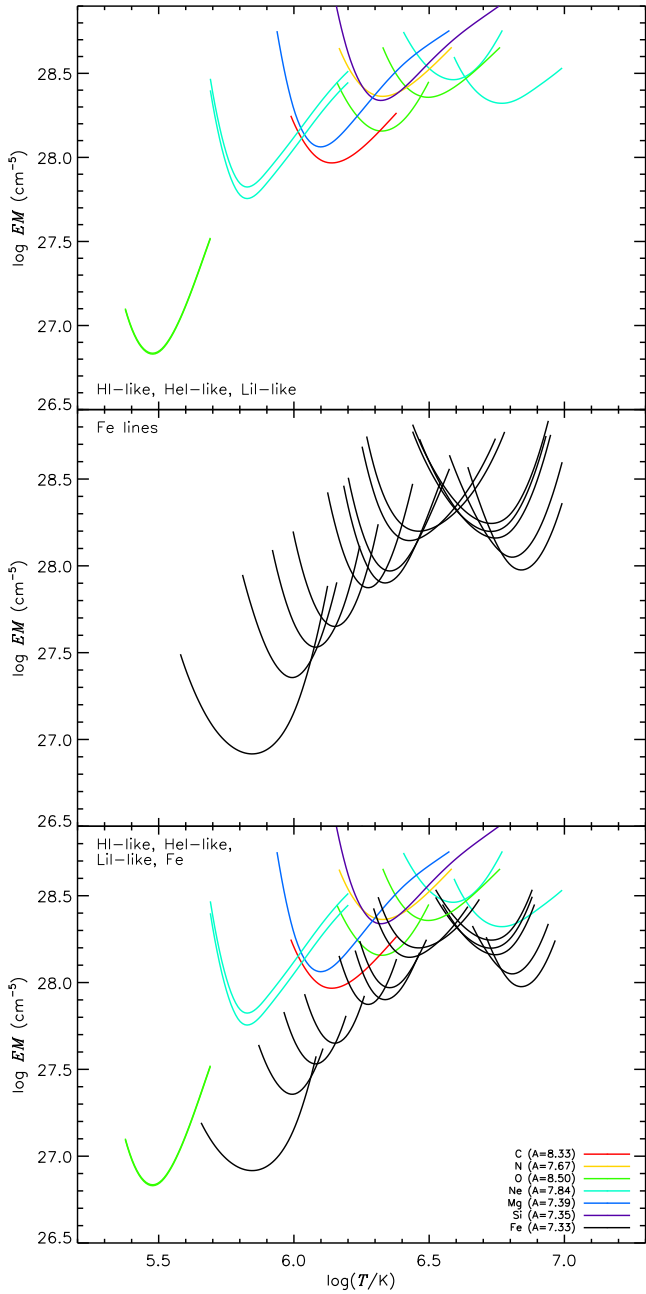


Figure 3. Emission Measure Loci for lines from the H I-like, He I-like and Li I-like isoelectronic sequences (top panel), lines of iron (middle panel), and all these lines (bottom panel). The photospheric abundances initially adopted for the transition region and corona of ϵ Eri are given in the bottom right legend. A value of $\log P_e = 16.10$ was adopted. The EMLs are apparent values - see Section 6.

formed over much smaller ranges of T_e than those from the above isoelectronic sequences. Because of these differences the impression that the relative abundance of iron adopted is *significantly* too large is not correct. However, from the top panel it appears that the adopted relative abundance of nitrogen and silicon is quite accurate, that the relative abundance of carbon and magnesium is too large and that the relative abundance of nitrogen and oxygen is too small.

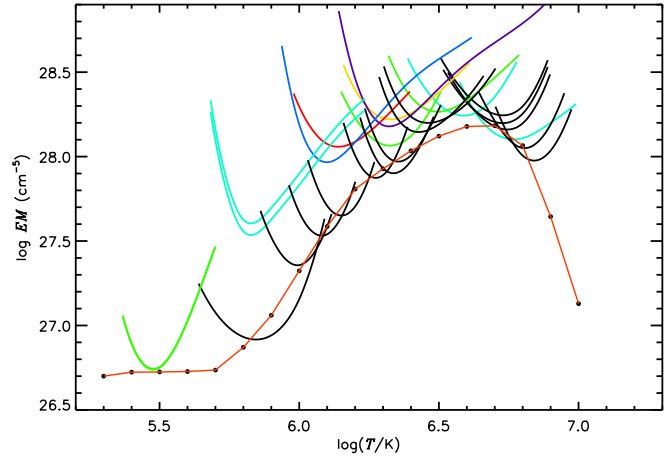


Figure 4. Emission Measure Loci for the most reliable lines, and the best-fit mean apparent emission measure ($EM(0.3)_{app}$ - see Section 6) (solid line with grid points). Here the final coronal abundances are used - see Table 8. A value of $\log P_e = 16.10$ was adopted.

From the bottom panel it appears that the relative abundance of neon and iron is too small.

To adjust the relative abundances, the mean EMD must be found and used to re-calculate the line fluxes; systematic differences in the calculated and observed fluxes for lines from the various elements can then be investigated. When attributing any differences to the effects of abundances, rather than to the shape of the EMD, it is assumed that the corrections to the abundances do not depend on T_e .

The mean EMD to be derived is defined in terms of the value of the emission measure for a logarithmic temperature range of 0.30 dex, hereafter, $EM(0.3)$. The value of P_e is assumed to be constant with T_e , and the results using the three values $\log P_e = 15.68, 15.30$ and 16.10 have been investigated.

In order to find an initial EMD the differences between the functions $g(n_e, T_e)$ for the lines used must be taken into account; some lines are formed over a small range of T_e , while others have contributions from a wide range of T_e . The procedure developed by Jordan & Wilson (1971) and applied, with some modification, by Griffiths & Jordan (1998) is adopted. First, the fraction of the line formed over a temperature range of $\log T_e = \log T_m \pm 0.15$ is calculated, where T_m is the temperature at which the line emissivity has its maximum value, *without* allowing for any variation of the EMD with T_e . The total contribution is found by integrating $g(n_e T_e)$ as a function of T_e , cutting off the integration when the value is 0.01 times the maximum value of $g(n_e T_e)$. Thus each locus of possible values of $EM(T_e)$ is replaced by one value, referring to the range $\Delta \log T_e = 0.3$ about $\log T_m$.

From the values of $EM(0.3)$ derived from each line it is then already clear that, relative to the lines of iron, the points for Ne VIII lie above the mean, i.e. the abundance of neon relative to iron is too small. At this point the de-blended fluxes of the lines of Ne X and Fe XVII discussed in Section 4.1 were used to derive a new starting abundance of 8.01 for neon. (See details in Section 5.3.) The individual

values from each line have then been used to define the initial mean distribution of $EM(0.3)$ with T_e .

This initial mean distribution, defined at intervals of 0.1 in $\log T_e$, is then iterated, taking into account the $g(n_e, T_e)$ functions over the full range of T_e used, and the effects of the variation of the EMD with T_e are now taken into account. The ratio of the observed to predicted fluxes is found and the iteration continued until these ratios do not change by more than 1 per cent.

The total flux in line j at step k , $F_{j,k}$, is given by

$$F_{j,k} = \sum_i EM(0.3)_{i,j,k} g_j(T_i) \frac{0.1}{0.3} \quad (3)$$

where i covers the temperature range over which the emissivity decreases to 0.01 of its maximum value and the notation for the g function has been abbreviated to $g_j(T_i)$.

At step k , the value of χ^2 , that indicates how good the fit is, is defined as

$$\chi_k^2 = \sum_j \frac{(F_{j,k} - F_{j,obs})^2}{F_{j,err}^2} \quad (4)$$

where $F_{j,k}$ is the flux predicted for line j , $F_{j,obs}$ is the observed flux in line j and $F_{j,err}$ is the error in the measured flux of line j .

The correction factor $CF_{j,k}$ required to bring the predicted flux into agreement with that observed in line j is defined as

$$CF_{j,k} = \frac{F_{j,k}}{F_{j,obs}} \quad (5)$$

This overall correction must be shared between the various values of T_i and so a weighted function,

$$CF_{i,j,k} = \frac{F_{j,k}}{F_{j,obs}} \frac{EM(0.3)_{i,k} g_j(T_i)}{\sum_i EM(0.3)_{i,k} g_j(T_i)} \quad (6)$$

is adopted. This allows for the differences between the $g_j(T_i)$ functions of the different lines and the variation of $EM(0.3)$ with T_i . The sum of the values of $\log CF_{i,j,k}$ is then found, including all lines used at a given i . Between each step, the values of $EM(0.3)_{i,k}$ are then corrected using

$$\log EM(0.3)_{i,k+1} = \log EM(0.3)_{i,k} + \frac{\sum_j \log CF_{i,j,k}}{n_i}, \quad (7)$$

where n_i is the number of lines included at T_i .

When the iteration process was completed, the systematic behaviour of the ratios of the observed and predicted fluxes for lines from the various elements were examined and small adjustments to the initial relative abundances adopted were made. We have found values relative to that of iron (as did Sanz-Forcada et al. 2004). The absolute values of the mean EMD will depend on the abundance of iron adopted. Sanz-Forcada et al. (2004) and Wood & Linsky (2006) derived absolute abundances of iron by measuring the line to continuum flux ratio, but we considered the continuum to be too weak for this to be useful; the error on the absolute abundance of iron found by Sanz-Forcada et al. (2004) is indeed quite large (7.20 ± 0.2). Wood & Linsky (2006) find a value of 7.35, very close to the value of 7.33 that we adopt. The mean EMD derived using the final relative abundances and $\log P_e = 16.10$ is shown in Fig. 4 by the solid line with the grid points. Fig. 4 also includes the loci for lines of isoelectronic sequences omitted from Fig. 3 for the sake of clarity.

The mean EMD has also been derived using $\log P_e = 15.30$ and 15.68, adopting the above relative abundances. These agree with that derived using $\log P_e = 16.10$ to within mean values of -0.03 and -0.02 dex, respectively. The largest differences occur between $\log T_e = 6.0$ and 6.2, where they are -0.07 dex (for $\log P_e = 15.30$) and -0.04 dex (for $\log P_e = 15.68$). Thus using a different value of P_e has an effect on the resulting mean EMD that is smaller than the uncertainties arising from the line flux measurements and the atomic data.

Alternatively, the relative abundances can be adjusted using the EMDs found with $\log P_e = 15.30$ and 15.68. For a fixed abundance of iron, these are on average 0.04 dex and 0.02 dex larger, respectively, than those derived using $\log P_e = 16.10$. Thus the abundances derived (see Section 5.3) do not depend significantly on the value of P_e used in deriving the mean EMD.

5.3 Relative coronal abundances

In Table 8 we give the stellar photospheric abundances according to Zhao et al. (2002), scaled from the solar photospheric abundances of Asplund et al. (2005). The coronal abundances derived from the tables in Sanz-Forcada et al. (2004) and Wood & Linsky (2006) are also given. The values that we derive are given in the final column, on a scale where the coronal abundance of iron is set equal to the stellar photospheric value. We have investigated the likely uncertainties in the coronal abundances in several ways. Because we determine these relative to a fixed value of the iron abundance, using the full set of maximum observed fluxes, or the full set of minimum observed fluxes, has very little effect on the abundances derived. Instead, we give the uncertainties that result when the maximum fluxes for the lines of iron are used, together with the minimum fluxes of all other lines, and vice-versa.

From Table 8 it can be seen that on the absolute scale adopted, all our abundances, except that for silicon, agree with those derived by Sanz-Forcada et al. (2004) to within our joint uncertainties. If their abundances are scaled to the photospheric abundance of iron (7.33), then all our abundances of elements used in finding the mean EMD agree with theirs, to within the joint uncertainties. Similarly, apart from those for oxygen and silicon, the abundances that we derive agree with those found by Wood & Linsky (2006).

Although we do not include the possible lines of Ni XII in deriving the mean EMD, we give the mean abundance that results, since nickel is a low FIP element. The lines of sulphur are all weak, and possibly blended, and individually give discordant abundances; the mean value is given. The possible line of Ca XII is predicted to be a factor of 4.2 weaker than that observed, and given the behaviour of the other low FIP elements there may be problems with the identification, the calibration or the atomic data. The possible blend between the Ca XI and S XIV lines at 30.45 Å does not appear to support such a large abundance of calcium. Using the observed to predicted fluxes for the other two lines of S XIV suggests an abundance of calcium of 6.46. We do not include calcium in the discussions below.

Given that the starting abundances used by ourselves, Sanz-Forcada et al. (2004) and Wood & Linsky (2006) are different, and that we have used more up-to-date atomic data and independent flux measurements, these comparisons

Table 8. Stellar photospheric abundances from Zhao et al. (2002), using Asplund et al. (2005) for the absolute scale; stellar coronal abundances derived by Sanz-Forcada et al. (2004), Wood & Linsky (2006) and from the present work (the latter being scaled to the stellar photospheric iron abundance).

| Element | Zhao et al. (2002) ^a | Sanz-Forcada et al. (2004) | Wood & Linsky (2006) ^b | This work ^b |
|-----------------|---------------------------------|----------------------------|--|--|
| C | 8.33 | 8.28 ± 0.18 | 8.15 ^{+0.04} _{-0.06} | 8.24 ^{+0.09} _{-0.07} |
| N | (7.67) ^c | 7.74 ± 0.14 | 7.71 ^{+0.04} _{-0.09} | 7.82 ^{+0.08} _{-0.07} |
| O | 8.50 | 8.53 ± 0.04 | 8.46 ^{+0.02} _{-0.03} | 8.59 ^{+0.04} _{-0.04} |
| Ne | (7.84) ^c | 8.09 ± 0.08 | 8.02 ^{+0.04} _{-0.02} | 8.06 ^{+0.09} _{-0.06} |
| Mg | 7.39 | 7.43 ± 0.10 | 7.46 ± 0.07 | 7.49 ^{+0.13} _{-0.13} |
| Si | 7.35 | 7.34 ± 0.07 | 7.33 ± 0.06 | 7.51 ^{+0.07} _{-0.07} |
| S ^d | 7.13 | 7.21 ± 0.15 | 7.15 ^{+0.14} _{-0.26} | 7.29 ^{+0.11} _{-0.15} |
| Ca ^d | 6.20 | 6.59 ± 0.20 | 6.70 ^{+0.25} _{-1.01} | (6.82 ^{+0.14} _{-0.16}) ^e |
| Fe | 7.33 | 7.20 ± 0.20 | 7.35 | [7.33] |
| Ni ^d | 6.13 | 6.24 ± 0.11 | 5.98 ^{+0.19} _{-0.62} | 6.14 ^{+0.08} _{-0.27} |

^a The likely errors in the relative abundances are as given in Table 7.

^b The errors are for the abundances relative to that of iron.

^c Not given by Zhao et al. (2002); values initially adopted here - see text.

^d Not used in determining the mean EMD.

^e The line involved is too weak to derive a reliable value.

show that a line-based approach to the analysis of X-ray data gives reproducible results.

However, the mean EMD that we derive differs from that found by Sanz-Forcada et al. (2004). Our EMD increases smoothly up to a peak value at around $\log T_e = 6.6$, whereas that found by Sanz-Forcada et al. (2004) has two peaks, at $\log T_e = 6.3$ and $\log T_e = 6.75 - 6.8$.

To test how well the EMD of Sanz-Forcada et al. (2004) reproduces the fluxes of the EUVE lines of Fe IX - Fe XII and Fe XIV included in our analyses, their volume EMD (that refers to intervals of 0.10 in $\log T_e$) has been converted to the scale of our EMD over height (that refers to intervals of 0.30 in $\log T_e$). The relative abundances derived are also examined for consistency between the various stages of ionization of a given element.

The EMD found by Sanz-Forcada et al. (2004) extends to only $\log T_e = 5.7$ and so cannot account for the fluxes in the O VI lines. Our EMD reproduces all the oxygen resonance lines well and the relative abundances found from these agree with each other to about a factor of 1.1. Similarly, apart from the resonance line of Fe IX and Fe XIII lines, our mean EMD leads to the same relative abundance of iron, to within a factor of 1.3, for all lines used in ions up to and including Fe XVIII. Sanz-Forcada et al. (2004) do not show observed to predicted fluxes for lines of ions between Fe XI and Fe XIV, so we assume that they did not include lines observed with the EUVE. We find that using their mean EMD gives relative iron abundances for these lines that depend on T_e and span a range of a factor of 2.6. Also, the abundances that we find from Ne VIII to X are more self-consistent. Thus, overall, we consider that our mean EMD gives a better representation of the line fluxes and relative abundances. The reason why we derive similar mean relative abundances to those found by Sanz-Forcada et al. (2004) appears to be the

influence of lines used in common in the higher temperature range where our mean EMDs are in closest agreement.

Wood & Linsky (2006) use a similar set of lines to those included by Sanz-Forcada et al. (2004), but adopt CHIANTI (v4.2) for the atomic data. The EMD that they find peaks at a similar temperature, but below $\log T_e = 6.0$ it is far smaller than ours, probably because they did not include the O VI lines observed with FUSE.

Since there is interest in the possible presence of a FIP (first ionization potential) effect, in which elements with a low FIP (less than about 10 eV) have relatively larger abundances in the corona, we have examined the relative abundances of oxygen and iron in the corona and photosphere, since this ratio has the smallest uncertainty in the corona. We derive a coronal value of $\log(n_O/n_{Fe}) = 1.26 \pm 0.04$. Combining the photospheric abundances of Asplund et al. (2005) and the differential abundances by Zhao et al. (2002) or Allende Prieto et al. (2004) leads to stellar photospheric values of $\log(n_O/n_{Fe}) = 1.17$ or 1.23, respectively. Similarly, adopting the solar photospheric abundances of Grevesse & Sauval (1998) leads to values of 1.29 or 1.35. Thus the largest difference between the photospheric and coronal relative abundances is ± 0.09 in the logarithm, and a larger relative abundance of iron in the corona is found only when the solar photospheric abundances of Asplund et al. (2005) are adopted. On the basis of observations made with the EUVE, Laming et al. (1996) concluded that any FIP effect in ϵ Eri was not significantly larger than that found in the solar corona. We conclude that there is no clear evidence for *any* FIP effect in the inner corona of ϵ Eri.

There is also considerable interest in the relative abundance of neon to oxygen, given its relevance to models of the solar interior (Bahcall et al. 2005) and the difficulties caused by the lower photospheric abundances of carbon, nitrogen, oxygen and neon in reconciling models with the results of helioseismology. From Table 8 it can be seen that the coronal value derived here is $\log(n_{Ne}/n_O) = -0.53$ (c/f -0.44 from Sanz-Forcada et al. 2004 or Wood & Linsky 2006). This ratio is significantly larger than the solar values of -0.82 and -0.75 recommended by Asplund et al. (2005) and Grevesse & Sauval (1998), respectively. It is also larger than the value of -0.77 found in the solar transition region by Young (2006), and is more similar to the mean stellar coronal value of -0.39 found by Drake & Testa (2005) (who used a more approximate method to find this ratio). The only obvious factors that could reduce the derived coronal abundance of neon would be the present limitations of the current atomic models for Ne VIII and perhaps Ne IX.

Abundances relative to that of iron can also be derived from de-blended lines, but these do depend on the accuracy of the combined atomic data for the lines used. When the Ne X and Fe XVII lines at 12.14 Å are deblended, the derived flux in the Ne X line is a factor of 1.09 smaller than that predicted. If this difference is attributed to an incorrect neon abundance then the abundance becomes 8.02, not 8.06. The predicted flux in the Fe XVII line at 12.29 Å is too small by a factor of 1.33, but we suspect that there are problems with the atomic data since the EMD based on the adopted abundance of 7.33 gives an overall fit to all the iron lines to within a smaller factor. Similarly, when the O VIII and Fe XVIII lines at 16.01 Å are deblended, the predicted flux in the O VIII line is too small, but only by a factor of 1.16. The

Table 9. The measured fluxes and the ratios of measured to predicted fluxes.

| Ion ^a | λ | F_{meas}^b | $\frac{F_{\text{meas}}^c}{F_{\text{pred}}}$ | Ion ^a | λ | F_{meas}^b | $\frac{F_{\text{meas}}^c}{F_{\text{pred}}}$ |
|------------------|---------------------|---------------------|---|------------------|---------------------|---------------------|---|
| C V | 40.27 | 3.35 | 1.14 ± 0.26 | Fe IX | 171.07 | 14.5 | 0.39 ± 0.04 |
| C VI | 33.74 | 17.1 | 1.03 ± 0.06 | Fe IX | 171.07 ^d | 21.1 | 0.56 ± 0.10 |
| N VI | 28.79 | 3.56 | 1.05 ± 0.16 | Fe X | 174.53 ^d | 20.5 | 1.07 ± 0.19 |
| N VII | 24.78 | 10.8 | 1.03 ± 0.08 | Fe XI | 180.41 ^d | 18.8 | 1.08 ± 0.21 |
| O VI | 150.12 | <2.3 | <1.0 | Fe XII | 193.67 ^d | 56.4 | 1.05 ± 0.42 |
| O VI | 1031.9 ^e | 45.9 | 1.04 ± 0.10 | Fe XII | 1242.0 ^f | 0.98 | 1.54 ± 0.11 |
| O VI | 1037.6 ^e | 22.6 | 1.03 ± 0.10 | Fe XII | 1349.4 ^f | 0.52 | 1.81 ± 0.52 |
| O VII | 21.60 | 41.5 | 0.98 ± 0.04 | Fe XIII | 203.83 ^d | 19.9 | 0.51 ± 0.19 |
| O VII | 21.81 | 9.59 | 1.28 ± 0.06 | Fe XIV | 211.32 ^d | 25.0 | 1.13 ± 0.20 |
| O VII | 22.10 | 27.3 | 1.11 ± 0.05 | Fe XV | 52.91 | 2.25 | 1.28 ± 0.21 |
| O VIII | 16.01 | 13.9 | 1.16 ± 0.06 | Fe XV | 59.40 | 2.99 | 1.38 ± 0.20 |
| O VIII | 18.97 | 88.2 | 1.00 ± 0.02 | Fe XV | 69.68 | 5.52 | 0.93 ± 0.07 |
| Ne VIII | 88.12 | 5.16 | 1.68 ± 0.29 | Fe XV | 73.47 | 2.73 | 1.24 ± 0.24 |
| Ne VIII | 98.12 | 1.72 | 1.00 ± 0.20 | Fe XV | 284.16 ^d | 104. | 0.86 ± 0.06 |
| Ne VIII | 98.27 | 4.00 | 1.17 ± 0.13 | Fe XVI | 50.36 | 3.54 | 2.41 ± 0.24 |
| Ne IX | 13.45 | 22.9 | 1.01 ± 0.05 | Fe XVI | 50.56 | 1.95 | 2.41 ± 0.27 |
| Ne IX | 13.55 | 7.57 | 1.97 ± 0.16 | Fe XVI | 54.13 | 2.86 | 2.12 ± 0.27 |
| Ne IX | 13.70 | 16.1 | 1.30 ± 0.07 | Fe XVI | 54.75 | 4.80 | 1.80 ± 0.17 |
| Ne X | 10.24 | 4.20 | 1.28 ± 0.23 | Fe XVI | 62.87 | 2.75 | 0.88 ± 0.14 |
| Ne X | 12.14 | 21.5 | 0.92 ± 0.04 | Fe XVI | 63.71 | 6.25 | 0.97 ± 0.09 |
| Mg IX | 72.31 | <1.2 | <1.3 | Fe XVI | 66.25 | 3.81 | 1.76 ± 0.23 |
| Mg IX | 77.74 | <0.6 | <0.9 | Fe XVI | 66.38 | 5.96 | 1.84 ± 0.19 |
| Mg X | 57.92 | 2.12 | 0.86 ± 0.19 | Fe XVI | 335.40 ^d | 85.9 | 0.93 ± 0.10 |
| Mg X | 63.31 | 2.82 | 1.02 ± 0.16 | Fe XVI | 360.75 ^d | 45.8 | 1.04 ± 0.10 |
| Mg X | 65.85 | 1.08 | 0.77 ± 0.25 | Fe XVII | 12.12 | 7.96 | 1.34 ± 0.06 |
| Mg XI | 9.17 | 12.6 | <1.7 | Fe XVII | 12.26 | 7.18 | 1.33 ± 0.15 |
| Mg XII | 8.42 | 3.68 | 1.55 ± 0.28 | Fe XVII | 13.82 | 3.67 | 0.89 ± 0.10 |
| Si X | 50.52 | 1.87 | 0.76 ± 0.07 | Fe XVII | 15.02 | 52.1 | 0.98 ± 0.03 |
| Si X | 50.69 | 2.84 | 0.65 ± 0.09 | Fe XVII | 15.26 | 21.8 | 1.45 ± 0.08 |
| Si XI | 43.76 | 2.90 | 2.13 ± 0.20 | Fe XVII | 16.78 | 30.4 | 1.02 ± 0.04 |
| Si XI | 49.22 | 3.81 | 1.34 ± 0.10 | Fe XVII | 17.05 | 77.0 | 1.13 ± 0.06 |
| Si XI | 52.30 | 2.17 | 1.00 ± 0.17 | Fe XVIII | 14.21 | 10.9 | 1.14 ± 0.10 |
| Si XII | 44.02 | 3.76 | 1.40 ± 0.11 | Fe XVIII | 16.01 | 3.25 | 1.03 ± 0.06 |
| Si XII | 44.18 | 5.48 | 1.03 ± 0.06 | Fe XVIII | 16.08 | 5.80 | 1.05 ± 0.12 |
| Si XII | 45.52 | 1.30 | 0.98 ± 0.16 | Fe XVIII | 93.92 | 7.24 | 1.04 ± 0.07 |
| Si XII | 45.69 | 2.02 | 0.75 ± 0.09 | Fe XVIII | 103.94 | 2.64 | 1.16 ± 0.18 |
| Si XIII | 6.65 | 8.4 | <2.0 | Fe XIX | 101.55 | 1.47 | 1.15 ± 0.28 |
| S XIII | 35.67 | 4.17 | 1.57 ± 0.21 | Fe XIX | 108.36 | 2.63 | 0.70 ± 0.11 |
| S XIV | 30.43 | 4.38 | 1.13 ± 0.17 | Fe XX | 132.84 | <4.0 | <1.5 |
| S XIV | 32.56 | 3.71 | 0.57 ± 0.09 | Ni XII | 152.15 | 3.06 | 0.95 ± 0.18 |
| Ca XII | 141.04 | 2.74 | 4.24 ± 0.88 | Ni XII | 154.16 | 1.71 | 1.10 ± 0.32 |

^aLines used in deriving the mean EMD are given in bold face.

^bFluxes in 10^{-14} erg cm⁻² s⁻¹, corrected for absorption in the ISM.

^cPredicted from the derived EMD, both using $\log P_e = 16.10$ (Fig. 4 and Table 10).

^dFluxes measured with *EUVE* (Schmitt et al. 1996).

^eFluxes measured with *FUSE* (Sim & Jordan 2005).

^fFluxes measured with STIS (Jordan et al. 2001a).

predicted flux in the Fe XVIII line at 16.07 Å is also too small, but by only a factor of 1.05. Thus, to within the expected uncertainties, the relative abundances from these individual lines are consistent with those derived from the overall fits.

Table 9 gives the measured line fluxes, corrected for absorption by the ISM, and the observed to predicted flux ratios for the lines used in deriving the mean EMD (shown in bold face), based on our abundances given in Table 8. The

flux ratios should be interpreted in the light of Section 4, where blending and atomic data issues are discussed.

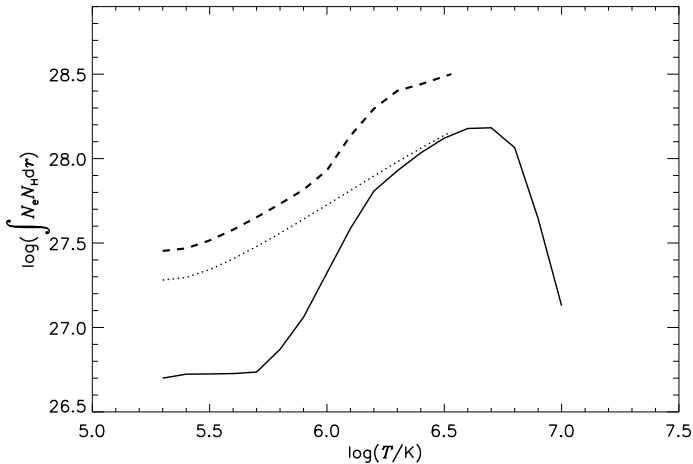


Figure 5. The distribution of $EM(0.3)_{\text{app}}$ derived from the measured line fluxes (full line); $EM(0.3)_{\text{cal}}$ derived from equations 8 and 9, using a spherically symmetric geometry (dotted line) and no fractional area factor; $EM(0.3)_{\text{cal}}A_*(r)/A(r)$ (dashed line). The calculated models have $\log T_c = 6.53$; see also Table 10.

6 MODELS BASED ON THE ENERGY BALANCE

The method used has been set out by Jordan & Brown (1981) for plane parallel geometry and for a spherically symmetric geometry by Pan & Jordan (1995). It has been extended by Sim & Jordan (2003a) to include emission from a restricted area at a given temperature and is only summarized here. Since the heating of the quiet corona occurs at heights much greater than the first pressure squared isothermal scale height over which the observed lines are predominantly formed, it is assumed that in the regions below, the divergence of the conductive flux is balanced by the local radiative losses. For a spherically symmetric atmosphere, with emitting area $A_*(r)$, and in hydrostatic equilibrium, the *theoretical* EMD is given by

$$\frac{d \log[EM(0.3)_{\text{th}}]}{d \log T_e} = \frac{3}{2} + 2 \frac{d \log P_e}{d \log T_e} + \frac{d \log A_*(r)}{d \log T_e} - \frac{2P_{\text{rad}}(T_e)EM(0.3)_{\text{th}}^2}{\kappa P_e P_H T_e^{3/2}}. \quad (8)$$

Here, $P_{\text{rad}}(T_e)$ is the radiative power-loss function and κ is the constant in the coefficient of thermal conductivity (the small variations in κ with T_e are ignored here). Equation (8) can be solved iteratively in hydrostatic equilibrium, to provide the run of the gas and electron pressures, the radial height and $EM(0.3)_{\text{th}}$ with T_e .

We only observe the ‘apparent’ emission measure, given by

$$EM(0.3)_{\text{app}} = EM(0.3)_{\text{th}} G(r) f(r) \frac{A(r)}{A_*(r)} \quad (9)$$

where $f(r) = (r/R_*)^2$ and $G(r)$ is the fraction of the photons emitted that are not intercepted by the star,

$$G(r) = 0.5(1 + \sqrt{1 - [1/f(r)]}). \quad (10)$$

When equation (8) is used $A_*/A(r)$, the fractional area occupied at a given r , is set equal to 1.0.

In solving equation (8) it is first assumed that $G(r) =$

1.0 and $f(r) = 1.0$, and the apparent value of the EMD at a chosen peak coronal temperature are used as boundary conditions. The starting value of the total gas pressure P_g is then found from these parameters and the isothermal pressure-squared scale height. The values of $G(r)$, $f(r)$ and the starting pressure are then updated in each iteration. Thus the iterated solution also provides the calculated apparent emission measure $EM(0.3)_{\text{cal}}$, which can be compared with that observed. The further boundary condition applied is that at the base temperature of $\log T_e = 5.3$, $d \log EM(0.3)_{\text{app}}/d \log T_e = 0$, to fit the overall observed mean EMD, including the results from Sim & Jordan (2005). If the solution is satisfactory, it will also reproduce the electron pressure of 15.97 ± 0.2 at $\log T_e = 5.3$.

Comparing $EM(0.3)_{\text{cal}}$ with $EM(0.3)_{\text{app}}$ allows any differences to be attributed to the effects of the emission originating mainly from a restricted area $A(r)$ at a given T_e . Additional terms can then be added to equation (8) to allow for $A(r)/A_*(r)$ and its variation with T_e . This results in eqn. (5) in Sim & Jordan (2003a), which gives the full expression for the gradient of $\log[EM(0.3)_{\text{cal}}A_*(r)/A(r)]$ with $\log T_e$. The values of $A(r)/A_*(r)$ can then be refined.

There are two differences between the application of the code used here and by Sim & Jordan (2003a). First, the maximum EMD is always associated with an isothermal region at the chosen coronal temperature, secondly, the form of $P_{\text{rad}}(T_e)$ adopted is $2.80 \times 10^{-19}/T_e^{1/2}$, to take account of the additional lines now included in atomic data bases.

After investigating a number of models using equation (8), the one that gives the best fit to the constraints set out above has a coronal temperature of $\log T_e = 6.53$, a peak emission measure of $\log EM(0.3)_{\text{cal}} = 28.16$ and a base pressure of $\log P_e = 15.97$. The EMD derived from the line fluxes and this solution for $EM(0.3)_{\text{cal}}$ are shown in Fig. 5 by full and dotted lines, respectively. The area factors derived are given in column 4 of Table 10.

Because of the form of the energy balance equation and the boundary conditions chosen, the choice of the coronal temperature determines the coronal emission measure and pressure. The ratio of the base pressure (at $\log T_e = 5.3$) to the coronal pressure has a constant value and the base pressure and temperature determine the theoretical value of the base $EM(0.3)$, and hence the fractional area at the base temperature. Thus the parameter space of the models can be further explored without additional full calculations. The scaling laws that result will be discussed by Jordan & Ness (in preparation).

The apparent EMD is poorly determined between $\log T_e = 5.3$ and 5.8, owing to the paucity of lines observed in this temperature range. When the derived areas are used in the full equation (5) of Sim & Jordan (2003a), the area is kept constant from $\log T_e = 5.3$ to 5.8, at the value at $\log T_e = 5.5$, where the lines of OVI are predominantly formed. This is justified by the small physical extent of this region. The resulting distribution of $\log[EM(0.3)_{\text{cal}}A_*(r)/A(r)]$ as a function of $\log T_e$ is shown in Fig. 5, and the new area factors that result are given in column 6 of Table 10. The radial extent and electron pressure in the final model are also given in Table 10. A further iteration with the new area factors was carried out to check that the new solution did not differ significantly from the previous one, but given the inherent uncertainties in the fluxes,

Table 10. The apparent and calculated EMDs, the fractional areas derived, the radial extent above $\log T_e = 5.3$ and P_e in the final theoretical models.

| $\log T_e$ (K) | $\log EM(0.3)_{\text{app}}^a$ | $\log EM(0.3)_{\text{cal}}^b$ | $[A(r)/A_*r]^c$ | $\log[EM(0.3)_{\text{cal}}A_*(r)/A(r)]^d$ | $[A(r)/A_*r]^e$ | $(r - r_0)^f$ 10^5 cm | P_e 10^{16} cm $^{-3}$ K |
|-------------------|-------------------------------|-------------------------------|-----------------|---|-----------------|----------------------------|---------------------------------|
| 5.30 | 26.700 | 27.281 | 0.26 | 27.453 | 0.18 | 0.0 | 1.38 |
| 5.40 | 26.724 | 27.296 | 0.27 | 27.468 | 0.18 | 5.4 | 1.40 |
| 5.50 | 26.725 | 27.343 | 0.24 | 27.515 | 0.14 | 1.44×10 | 1.41 |
| 5.60 | 26.727 | 27.406 | 0.21 | 27.579 | 0.14 | 3.04×10 | 1.43 |
| 5.70 | 26.736 | 27.479 | 0.18 | 27.653 | 0.12 | 5.98×10 | 1.43 |
| 5.80 | 26.871 | 27.558 | 0.21 | 27.732 | 0.14 | 1.15×10^2 | 1.44 |
| 5.90 | 27.061 | 27.641 | 0.26 | 27.816 | 0.18 | 2.19×10^2 | 1.44 |
| 6.00 | 27.324 | 27.726 | 0.40 | 27.931 | 0.25 | 4.29×10^2 | 1.43 |
| 6.10 | 27.586 | 27.812 | 0.59 | 28.136 | 0.28 | 9.32×10^2 | 1.41 |
| 6.20 | 27.808 | 27.897 | 0.81 | 28.295 | 0.33 | 2.16×10^3 | 1.37 |
| 6.30 | 27.928 | 27.981 | 0.89 | 28.402 | 0.34 | 4.87×10^3 | 1.30 |
| 6.40 | 28.034 | 28.061 | 0.94 | 28.440 | 0.39 | 1.03×10^4 | 1.20 |
| 6.50 | 28.121 | 28.138 | 0.96 | 28.487 | 0.43 | 2.09×10^4 | 1.07 |
| 6.53 | 28.138 | 28.158 | 0.95 | 28.500 | 0.43 | 2.58×10^4 | 1.02 |

^a Derived using $\log P_e = 16.10$.

^b Calculated with $A(r)/A_*(r) = 1.0$.

^c Fractional areas calculated from columns 2 and 3.

^d Calculated including a variable area factor.

^e Fractional areas calculated from columns 2 and 5.

^f Radial distance above $r = 5.18 \times 10^{10}$ cm at $\log T_e = 5.30$.

atomic data and the constants used in the energy balance equation, a fully converged solution was not pursued.

The mean EMD derived directly from the observed line fluxes peaks at a temperature around $\log T_e = 6.6 \pm 0.05$ and the lines of Fe XVIII and to a lesser extent, Fe XVII, do appear to require material at higher temperatures. We attribute this emission to active regions, but cannot model them to remove their contribution, since the electron pressure is not known, and the energy balance used here will not be appropriate, since heating by other than thermal conduction is not included. Quiet coronal models with $\log T_e \geq 6.6$ that satisfy the constraint on the emission measure gradient at $\log T_e = 5.3$ lead to base values of $\log P_e$ that exceed the upper limit of 16.17 derived from the density-sensitive lines at about this temperature.

It is difficult to make detailed comparisons with other earlier work, but there are several early determinations of the temperature at which the peak EMD occurs. Giampapa et al. (1985) used observations of ϵ Eri made with the Imaging Proportional Counter (IPC) on the *Einstein Observatory* to deduce a single-temperature fit of $\log T_e = 6.53$, close to the value of 6.60 (± 0.05) at which we and Wood & Linsky (2006) find the EMD to peak. However, the loop models that Giampapa et al. (1985) investigated had pressures that exceeded those found here and they remark that they could not simultaneously explain the IUE and X-ray spectra. Schmitt et al. (1990) also used these observations but could not find a single-temperature fit to the spectrum. The two-temperature fit that they suggested is not consistent with the present results. Because there was some suggestion that the absence of stars with coronal temperature (T_c) between $\log T_e = 6.67$ and 6.88 in the sample studied by Schmitt et al. (1990), might arise from the energy response function of the IPC, Montesinos & Jordan (1993) used their scaling law between T_c , g_* and the Rossby num-

ber, Ro , to predict the coronal temperature for ϵ Eri. With the currently adopted value of g_* , the scaling law predicts $\log T_e = 6.57$, close to the value found here. The emission measures shown by Laming et al. (1996), based on observations with the *EUVE*, also peak at $\log T_e = 6.5 \pm 0.1$. Thus there is good agreement between the peak temperature from the observations made with three different instruments.

The absolute scale of $EM(0.3)_{\text{app}}$ that we adopt depends on the value of the iron abundance used. If a smaller value were used, the values of $EM(0.3)_{\text{app}}$ would all increase. The intercept with $EM(0.3)_{\text{cal}}$ would occur at a lower temperature and above this value, the area factors would exceed 1.0, which is not physically acceptable. Thus it seems unlikely that the adopted value of the iron abundance is significantly too large. Conversely, using a larger iron abundance would lead to smaller values of $EM(0.3)_{\text{app}}$. This would result in smaller values of $A(r)/A_*(r)$ by the same factor. Such solutions cannot be excluded.

7 DISCUSSION AND CONCLUSIONS

We have analysed line fluxes measured with the LETGS on *Chandra* to obtain an apparent EMD. As part of this work we have examined the self-consistency of the results from lines of a given ion. There remain inconsistencies in the results from different lines of Fe XVI and, to a lesser extent, Fe XV. One source of these differences could be excitations to n-states not yet included in the atomic models, followed by cascades. Although the lines are weak, there is a significant difference between the observed and predicted fluxes for the $3p - 2s$ transition in Ne VIII. The atomic models and data do not appear to have been updated in CHIANTI since v3. There also needs to be a proper treatment of recombination (including cascades) to the $1s2s$ 3S level in the He I-like ions

and di-electronic recombination needs to be included. The pressure indicated by the f/i ratio in O VII is currently somewhat larger than expected from the final model. Although blends have been taken into account in analysing the Fe XIII lines at around 203.8 Å the observed flux is lower than predicted by CHIANTI (v5.2), unless $\log P_e$ is lower than 15.30, which is not consistent with the results from other lines.

Line optical depths can be estimated using the final model that includes the variable area factors. Several lines, in particular the resonance line of Fe IX at 171 Å, are estimated to have line-centre optical depths approaching 1. The effects on the measured fluxes will depend on the geometry; scattering *out of* the line of sight would be expected for lines formed in supergranulation boundaries, but to find the expected flux when integrated over the whole star would require detailed radiative transfer calculations.

Relative element abundances have been determined in the upper transition region/corona. These agree with those found previously by Sanz-Forcada et al. (2004) to within the expected uncertainties, and quite well with those of Wood & Linsky (2006), in spite of differences in the mean EMDs. This reproducibility lends support to the individual line-based methods of deriving abundances. The EMD found here is based on line fluxes measured from the LETGS spectrum, the STIS spectrum (for O VI) and on the *EUVE* counts measured by Schmitt et al. (1996) for Fe IX to XII and Fe XIV to XVI. This EMD gives a consistent relative element abundance of iron for all stages of ionization included, apart from Fe IX, for which the line flux is observed to be weaker than predicted. Using the EMD found by Sanz-Forcada et al. (2004) leads to a larger difference between the abundances found from Fe XI, XII and XIV. On the basis of the relative abundances of oxygen and iron, we conclude that there is no clear evidence of any difference between photospheric and coronal abundances for low and high FIP elements. Indeed, none of our previous studies of stellar transition regions has shown any clear evidence of FIP effects. The spatially integrated X-ray line fluxes are dominated by the first pressure-squared isothermal scale height; if changes in relative element abundances are occurring at greater heights in the corona, they might not be detectable. (See also discussion by Wood & Linsky 2006 regarding correlations with stellar mass-loss rates.)

The important Ne/O relative abundance is found to be -0.53 (on a logarithmic scale), slightly smaller than the value of -0.44 found by Sanz-Forcada et al. (2004) and Wood & Linsky (2006), but larger than the values of -0.82 and -0.75 recommended by Asplund et al. (2005) and Grevesse & Sauval (1998), respectively, for the solar atmosphere. It is also larger than that found for the solar transition region by Young (2006) (-0.77). Drake & Testa (2005) derived an even larger value (-0.39) from studies of a range of active stars, but used a more approximate method, not a full study of the EMD. Since the relative abundances of O and Fe found in the stellar corona agree with the range of stellar photospheric values to within ± 0.09 in the logarithm, it appears that it is the abundance of Ne in the stellar corona that differs from the recommended solar values. Drake & Testa (2005) have suggested that a larger Ne/O abundance ratio could resolve the difficulties introduced by the adoption of the lower C, N, and O abundances proposed by Asplund et al. (2005).

The similarity of the variation of the EMD with T_e found by using lines from individual isoelectronic sequences or just one element can be seen from Figs. 3 and 4. We are of the opinion that line-based analyses, using the full emission measure contribution functions is the best method for determining the mean EMD.

Recent work by the other authors mentioned above has concentrated on deriving a mean EMD and element abundances but models of the atmosphere were not produced. We regard the main purpose of deriving the mean EMD is to use it in comparisons with theoretical models based on assumptions about the energy balance. Early work on modelling in terms of loop structures was not entirely successful (e.g. that by Giampapa et al. 1985). We intend to study a larger sample of stars in future work, to investigate the systematic behaviour with stellar activity.

The mean (apparent) EMD has been compared with the predictions of models based on the assumption of an energy balance between the divergence of the thermal conductive flux and the radiation losses. This allows the fractional area of the emitting material to be found as a function of T_e . When the variation of the fractional area is not included, we find a fractional area that is constant at about 0.24 up to $\log T_e = 5.8$ and then increases with T_e to reach about 1 by $\log T_e = 6.4$. Allowing for the variation of the fractional area with T_e increases the calculated values of P_e and reduces the base fractional to 0.14 and the coronal area factor to 0.43. The solutions derived here do not have the problem of fractional areas that are greater than 1 that occurred in the earlier analyses by Sim & Jordan (2005). The derived behaviour is similar to the trend in the area occupied by the supergranulation network boundaries in the solar transition region and inner corona, taking into account that the stellar transition region extends to higher temperatures, because the coronal temperature is higher. At the lower end of the temperature range, the surrounding material would be at near coronal temperatures; the coronal filling factor of less than one is consistent with the additional presence of active regions.

ACKNOWLEDGMENTS

J.-U.N acknowledges support from PPARC under grant number PPA/G/S/2003/00091 and from NASA through *Chandra* Postdoctoral Fellowship grant PF5-60039 awarded by the *Chandra* X-ray Center, which is operated by the Smithsonian Astrophysical Observatory for NASA under contract NAS8-03060. We thank the referee for useful comments on photospheric abundances.

REFERENCES

- Abia C., Rebolo R., Beckman J. E., Crivellari L., 1988, *A&A*, 206, 100
- Allende Prieto, C., Barklem, P. S., Lambert, D. L., & Cunha, K. 2004, *A&A*, 420, 183
- Anders E., Grevesse N., 1989, *Geochim. Cosmochim. Acta*, 53, 197
- Arnaud M., Raymond J., 1992, *ApJ*, 398, 394
- Arnaud M., Rothenflug R., 1985, *A&AS*, 60, 425

- Asplund M., Grevesse N., Sauval A. J., 2005, in III T. G. B., Bash F. N., (eds), ASP Conf. Ser. 336, Cosmic Abundances as Records of Stellar Evolution and Nucleosynthesis ASP, San Francisco, p. 25
- Bahcall J. N., Basu S., Pinsonneault M., Serenelli A. M., 2005, ApJ, 618, 1049
- Baliunas S. L., Hartmann L., Noyes R. E., Vaughan H., Preston G. W., Frazer J., Lanning H., Middelkoop F., Mihalas S., 1983, ApJ, 275, 752
- Baliunas S. L. et al., 1995, ApJ, 438, 269
- Binello A. M., Landi E., Mason H. E., Storey P. J., Brosius J. W., 2001, A&A, 370, 1071
- Blumenthal G. R., Drake G. W. F., Tucker W. H., 1972, ApJ, 172, 205
- Bodaghee A., Santos N. C., Israelian G., Mayor M., 2003, A&A, 404, 715
- Brickhouse N. S., Schmelz J. T., 2006, ApJ, 636, L53
- Brown G. V., et al., 2006, Phys Rev Lett, 96, 253201
- Chung S. M., Drake J. J., Kashyap V. L., Ratzlaff P. W., Wargelin B. J., 2004, in Flanagan K. A., Siegmund O. H. W., (eds), SPIE Vol. 5165, X-Ray and Gamma-Ray Instrumentation for Astronomy XIII, SPIE Homepage <http://spie.org/>, p. 518
- Cornille M., Dubau J., Mason H. E., Blancard C., Brown W. A., 1997, A&A, 320, 333
- Dere K. P., Landi E., Mason H. E., Monsignori Fossi B. C., Young P. R., 1997, A&AS, 125, 149
- Di Folco E., Thévenin F., Kervella P., Domiciano de Souza A., Coudé du Foresto V., Ségransan D., Morel P., 2004, A&A, 426, 601
- Di Folco E., et al., 2007, A&A, 475, 243
- Donahue R. A., Saar S. H., Baliunas S. L., 1996, ApJ, 466, 384
- Drake J., 2004, Chandra News, 11, 8
- Drake J. J., Smith G., 1993, ApJ, 412, 797
- Drake J. J., Testa P., 2005, Nature, 436, 525
- Dring A. R., Linsky J., Murthy J., Henry R. C., Moos W., Vidal-Madjar A., Audouze J., Landsman W., 1997, ApJ, 488, 760
- Eissner W., Galavís M. E., Mendoza C., Zeippen C. J., 1999, A&AS, 136, 385
- ESA, 1997, ESA SP-1200, The *Hipparcos* and *Tycho* Catalogue, ESA, Noordwijk
- Gabriel A. H., Jordan C., 1969, MNRAS, 145, 241
- Gabriel A. H., Jordan C., 1973, ApJ, 186, 327
- Gabriel A. H., Jordan C., 1975, MNRAS, 173, 397
- Giampapa M. S., Golub L., Peres G., Serio S., Vaiana G., 1985, ApJ, 289, 203
- Greaves J. S. et al., 2005, ApJ, 619, L187
- Grevesse N., Sauval A. J., 1998, Space Sci Rev, 85, 161
- Griffiths N. W., Jordan C., 1998, ApJ, 497, 883
- Hatzes A. P. et al., 2000, ApJ, 544, L145
- Heroux L., Cohen M., Malinovsky M., 1972, SolPhys, 23, 369
- Jordan C., 1965, Phys.Lett, 18, 259
- Jordan C., Brown A., 1981, in Bonnet R. M., Dupree A. K., (eds), NATO ASIC 68, Solar Phenomena in Stars and Stellar Systems, Reidel, Dordrecht. p. 199
- Jordan C., Wilson R., 1971, in Macris C. J., (ed.), Physics of the Solar Corona, Reidel, Dordrecht, p. 219
- Jordan C., McMurry A. D., Sim S. A., Arulvel M., 2001a, MNRAS, 322, L5
- Jordan C., Sim S. A., McMurry A. D., Arulvel M., 2001b, MNRAS, 326, 303
- Keenan F. P., Drake J. J., Chung S., Brickhouse N. S., Aggarwal K. M., Msezane A. Z., Ryans R. S. I., Bloomfield D. S., 2006, ApJ, 645, 597
- Kelly R. L., 1987, J. Phys. Chem. Ref. Data, Vol. 16, Suppl. No. 1, NBS, Gaithersburg
- Kurucz R., 1993, CD-ROM No. 13, ATLAS9 Stellar Atmospheres Program and 2 km s⁻¹ Grid, Smithsonian Astrophys. Obs., Cambridge
- Laming J. M., Drake J. J., Widing K. G., 1996, ApJ, 462, 948
- Landi E., Del Zanna G., Young P. R., Dere K. P., Mason H. E., Landini M., 2006, ApJS, 162, 261
- Montesinos B., Jordan C., 1993, MNRAS, 264, 900
- Ness J.-U., Wichmann R., 2002, Astronomische Nachrichten, 323, 129
- Ness J.-U., Mewe R., Schmitt J. H. M. M., Raassen A. J. J., Porquet D., Kaastra J. S., van der Meer R. L. J., Burwitz V., Predehl P., 2001, A&A, 367, 282
- Ness J.-U., Schmitt J. H. M. M., Burwitz V., Mewe R., Raassen A. J. J., van der Meer R. L. J., Predehl P., Brinkman A. C., 2002, A&A, 394, 911
- Ness J.-U., Schmitt J. H. M. M., Audard M., Güdel M., Mewe R., 2003a, A&A, 407, 347
- Ness J.-U., Brickhouse N. S., Drake J. J., Huenemoerder D. P., 2003b, ApJ, 598, 1277
- Pan H. C., Jordan C., 1995, MNRAS, 272, 11
- Porquet D., Dubau J., 2000, A&AS, 143, 495
- Raassen A. J. J., Mewe R., Audard M., Güdel M., Behar E., Kaastra J. S., van der Meer R. L. J., Foley C. R., Ness J.-U., 2002, A&A, 389, 228
- Raassen A. J. J., Ness J.-U., Mewe R., van der Meer R. L. J., Burwitz V., Kaastra J. S., 2003, A&A, 400, 671
- Rüedi I., Solanki S. K., Mathys G., Saar S. H., 1997, A&A, 318, 429
- Sanz-Forcada J., Brickhouse N. S., Dupree A. K., 2003, ApJS, 145, 147
- Sanz-Forcada J., Favata F., Micela G., 2004, A&A, 416, 281
- Schmitt J. H. M. M., Collura A., Sciortino S., Vaiana G. S., Harnden F. R., Rosner R., 1990, ApJ, 365, 704
- Schmitt J. H. M. M., Drake J. J., Stern R. A., Haisch B. M., 1996, ApJ, 457, 882
- Sim S. A., Jordan C., 2003a, MNRAS, 346, 846
- Sim S. A., Jordan C., 2003b, MNRAS, 341, 517
- Sim S. A., Jordan C., 2005, MNRAS, 361, 1102
- Smith R. K., Brickhouse N. S., Liedahl D. A., Raymond J. C., 2001, ApJL, 556, L91
- Storey P. J., Del Zanna G., Mason H. E., Zeippen C. J., 2005, A&A, 433, 717
- Wood, B. E., & Linsky, J. L. 2006, ApJ, 643, 444
- Young P. R., 2006, in Lacoste, H. and Ouwehand, L., (eds), ESA SP-617, The Solar Neon Abundance and the Standard Solar Model, ESA, Noordwijk, p. 47
- Young P. R., Del Zanna G., Landi E., Dere K. P., Mason H. E., Landini M., 2003, ApJS, 144, 135
- Zhao G., Chen Y. Q., Qiu H. M., Li Z. W., 2002, AJ, 124, 2224